Recent progress in films with nanoengineered surfaces via bubble-induced self-assembly for energy applications

Ben Chu [a], Benwei Fu [a, *], Ruitong Wang [a], Weizheng Cheng [a], Peng Tao [a], Chengyi Song [a], Wen Shang [a], Tao Deng [a, *]

a. State Key Laboratory of Metal Matrix Composites, School of Materials Science and Engineering, Shanghai Jiao Tong University, Shanghai 200240, P.R. China.

*Corresponding authors: Benwei Fu, email: fuwei880603@sjtu.edu.cn

Tao Deng, email: dengtao@sjtu.edu.cn

Abstract

Films with nanoengineered surfaces have been extensively utilized in a variety of energy-related applications such as water desalination, thermal management and solar steam generation. To generate high-quality films, various generation methods including chemical vapor deposition, electrodeposition and microlithography have been studied. Compared to these methods, however, bubble-induced self-assembly (BISA) has been developed as an alternative strategy due to the advantages of being facile and cost-effective, and triggered considerable research efforts. In this review, we overview recent advances in the development of films with nanoengineered surfaces via the BISA of nanomaterials. The mechanism and regulation of the BISA to generate high-performance films with desired surface characteristics are discussed in detail. We also highlight the application of the BISA strategy for enhanced phase-change heat transfer. Additionally, other applications of the BISA strategy are described, which range from effective thermal management of electronics and concentrated photovoltaics to advanced energy storage and conversion. Finally, we discuss the current challenges and potential research directions in the field. It is expected that this review will provide a comprehensive understanding of the design, generation, applications and perspectives of films with nanoengineered surfaces generated by the BISA.

Keywords: self-assembly, phase-change heat transfer, nanoengineered surface, thermal energy management, advanced energy storage

Nomenclature

q_{CHF}	critical heat flux ($kW \cdot m^{-2}$)
h_{fg}	latent heat of working medium ($J \cdot kg^{-1}$)
Ra	roughness parameter
g	gravitational acceleration ($m^2 \cdot s^{-1}$)
Cp	specific heat capacity ($J \cdot kg^{-1} \cdot K^{-1}$)
A_b	surface area of boiling surface (mm^2)
V_w	liquid wicking rate ($mm \cdot s^{-1}$)

Greek symbols

ρ_v	density of vapor ($kg \cdot m^{-3}$)
ρ_l	density of liquid ($kg \cdot m^{-3}$)
σ	surface tension ($N \cdot m^{-1}$)
β	Inclination (degrees)
α	contact angle (degrees)
θ_r	receding angle (degrees)

1. Introduction

With the increase of population and development of economy in modern society, energy issue has been arising extensive attention.[1-3] To meet global energy demand and achieve carbon neutrality, it is desired that energy can be utilized with improved efficiency.[4] Bubble, a common and fascinating substance in human life and engineering fields, usually serves as an efficient energy carrier.[5] Generally, bubbles can be readily generated by boiling, which is a kind of phase-change heat transfer and uses the enormous vaporization latent heat of phase-change working medium to dissipate high heat flux.[6-8] This ubiquitous boiling process has been an economical, attractive and efficient technology for energy utilization, and found immense utility in practical industrial applications, such as power plant,[9] heat exchanger,[10] nuclear reactor,[11] concentrated photovoltaics,[12] and high-power-density electronic cooling[13].

The overall boiling process consists of the convection, nucleation boiling, transition and film boiling,[14-19] and two key parameters including critical heat flux (CHF) and heat transfer coefficient (HTC) reflect the boiling heat transfer capacity.[20-25] The CHF expresses the maximum heat flux that boiling surface can withstand, while the HTC describes the capability of heat dissipation. Theoretically, the boiling heat transfer capacity is mainly related to the thermal physical properties of working medium and characteristics of boiling surfaces.[26-28] Due to the limitation in choice of working medium in a boiling system, recent researches have paid more attention to building up films with nanoengineered surfaces to modify the characteristics of substrates for enhancing boiling heat transfer by micro/nanofabrication technologies.[29-31] Conventional fabrication technologies such as the high-precision milling,[32] wire cutting,[33] high-temperature sintering,[34] and electrochemical deposition,[35] as well as the emerging fabrication technologies including the chemical vapor deposition (CVD),[36] layer-by-layer deposition,[37] additive manufacturing,[38] microlithography,[39] and evaporation-induced self-assembly (EISA)[40, 41] have been used to generate different patterned micro/nanostructures. Some of these preparation technologies, however, require quite complex procedures, considerable time and expensive equipment.

To solve above challenges, a facile, scalable and cost-effective bubble-induced self-assembly (BISA) method has been developed. Loading only a small number of nanomaterials within nanofluid as the working medium for boiling can result in the deposition and self-assembly of nanomaterials to generate films with nanoengineered surfaces on the substrate underneath bubbles.[42] Briefly, this BISA approach mainly uses the mechanism of the rapid microlayer evaporation of liquid under bubbles.[43] Recently, various nanomaterials, such as the metal-based nanoparticles,[44, 45] inorganic nonmetallic nanoparticles,[46] and carbon-based nanomaterials,[47-49] have been used for the BISA to generate different films with nanoengineered surfaces. Additionally, films with nanoengineered surfaces can directly be generated on different substrates including metal, polymer, silicon and glass. Besides the utilization for vapor-liquid phase-change heat transfer, these generated films have been used for a variety of applications, which include the efficient energy storage, thermal management for high-heat-flux electronics and smart sensors. This developed BISA strategy provides an alternative choice to fabricate high-performance films and structured surfaces on the target substrate. Despite the great efforts in researches of the BISA, a detailed and clear review to have a comprehensive understanding of the BISA is still lacking.

In this paper, we first review recent advanced researches in films with nanoengineered surfaces by the BISA method (Fig. 1). Subsequently, the fundamental mechanism of the BISA is deeply illustrated. The ways of tuning surface structures and characteristics by regulating parameters of the BISA process are introduced in detail. Recent efforts to generate high-performance films with desirable surface characteristics for enhanced phase-change heat transfer are presented. We also discuss the films generated by the BISA on various flat substrates and structured surfaces, and summarize their properties and potential energy-related applications. Finally, some challenges of the BISA strategy are outlined, and the future direction for improving the BISA, which may be worthy of further investigation, are discussed.

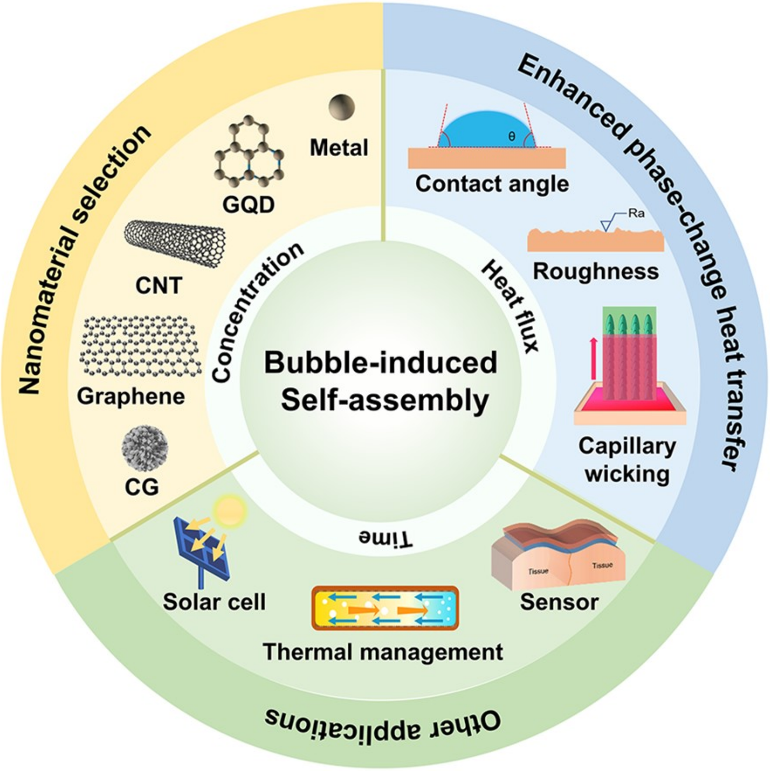

Fig. 1. Overview of regulation of the BISA to generate films with nanoengineered surfaces for enhanced phase-change heat transfer and other energy-related applications.

2. Fundamental mechanism of the BISA

It is considerably crucial to understanding the fundamental mechanism of the BISA for generating various films with nanoengineered surfaces. The BISA is achieved by controlling heat-generated microbubble nucleation and growth at the liquid-substrate interface when nanofluid containing nanomaterials is used as working medium (Fig. 2a). When enough heat flux is supplied to the substrate, individual bubble nucleates and grows on the surface during the nucleate boiling. Under the bubble there exist three regions, including the non-evaporation region, the evaporating thin film region and the bulk region from the center to the edge of the bubble, respectively.[50] The rapid liquid evaporation, which happens in the evaporating thin film region with the thickness from nearly zero to several micrometers underneath individual bubble, enables the accumulation and self-assembly of nanomaterials.[43]

"What forces facilitate the film generation by the BISA" is one of the basic questions in the BISA. The specific physical forces in the evaporating thin film region during boiling, which contribute to the BISA of nanomaterials, have been shown in Fig. 2b. With the continuous liquid evaporation, the nanofluid containing nanomaterials is replenished from the bulk region to rewet the evaporating thin film region due to the capillary force (F_{cap}).[51] The structural disjoining pressure (F_{Π}), which is defined as the excess pressure in the thin liquid film compared to that in the bulk liquid, participates in the BISA of the nanomaterials.[52] Furthermore, the vapor recoiling force (F_v) also squeezes the evaporating thin film region during the bubble growth, which facilitates the self-assembly of nanomaterials (Fig. 2c).[53, 54] These forces generated in the evaporating thin film region enable the BISA of nanomaterials to fabricate films with nanoengineered surfaces on the substrate.

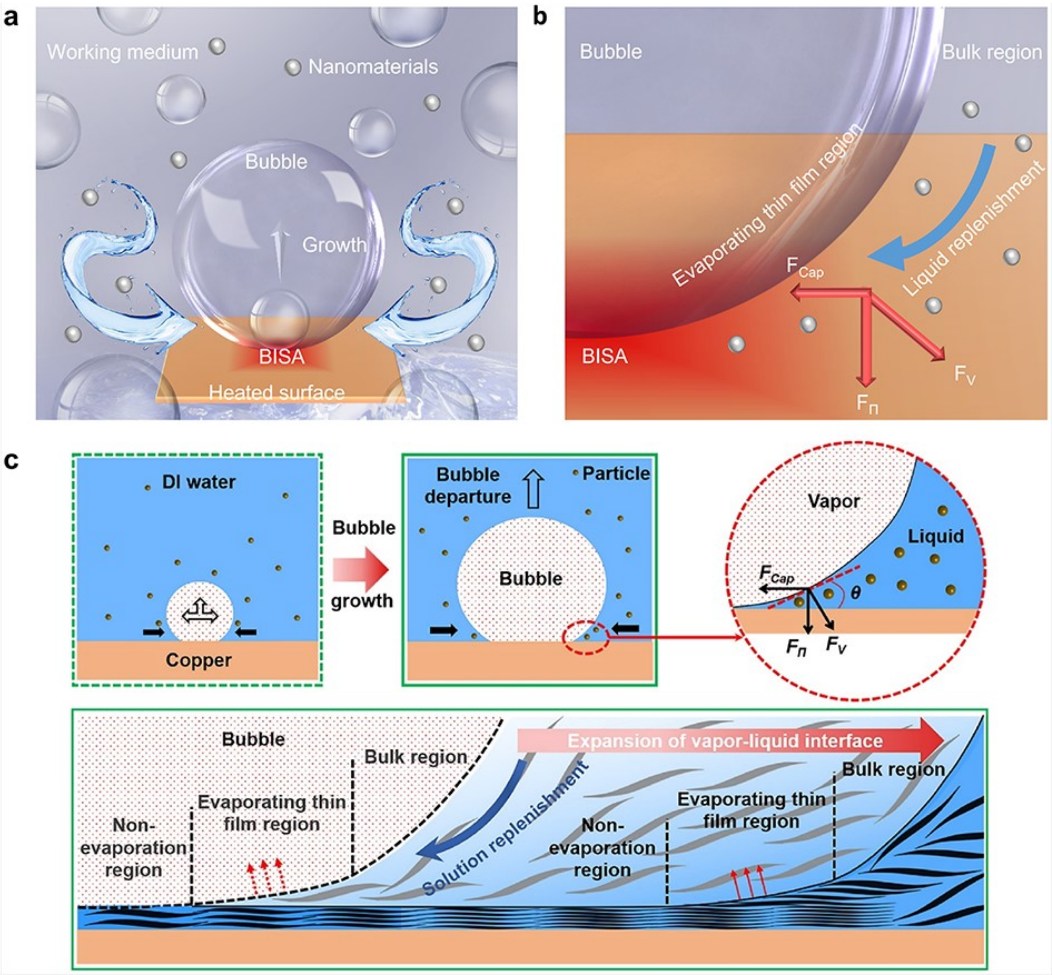

Fig. 2. Fundamental mechanism of the BISA. (a) Schematic diagram of the BISA process of nanomaterials. Mechanism of the BISA underneath an individual bubble. (b) Forces acting on the evaporating thin film region include the capillary force (F_{Cap}), vapor recoil force (F_v), and force due to structural disjoining pressure (F_{Π}). (c) Self-assembly and deposition of graphene-based nanomaterials with the bubble growth during the BISA. Reproduced with permission.[43] Copyright 2021, Elsevier.

3. Regulation of the BISA to generate different films with nanoengineered surfaces

The surface characteristics of films fabricated by the BISA can be tuned by loading various nanomaterials with different shape, size and wettability. In addition, the BISA process involves mainly the generation and growth of bubbles on the heated surface. Through regulating the bubble dynamic behaviors, the BISA can be tunable to generate favorable films with nanoengineered surfaces. Hence, several factors determining the characteristics of films generated by the BISA are the selection of nanomaterials, concentration of the added nanomaterials in nanofluid as boiling working medium, self-assembly duration, and applied heat flux for the BISA, respectively.

3.1 Nanomaterials

The selection of nanomaterials for the BISA can determine surface structures and characteristics of the generated films. Many recent efforts have been devoted to loading various nanomaterials of different dimensions, including the 0-dimensional (0D) metal oxide nanoparticles and graphene quantum dot (GQD),[55, 56] one-dimensional (1D) carbon nanotubes (CNTs),[57] 2D graphene-based nanomaterials,[58] and three-dimensional (3D) crumpled graphene (CG),[59] into various boiling working medium for the BISA to generate films with nanoengineered surfaces.[60] The SEM images of the films fabricated by the BISA using these nanomaterials are shown in Fig. 3, respectively. 0D nanomaterials with considerably small size, such as alumina[61] and maghemite[62] nanoparticles, were loaded in the solution to generate thin and uniform films during the BISA, respectively (Fig. 3a and 3b). The thin films with nanostructured surfaces deposited by the BISA helped provide a large quantity of bubble nucleation and reduce the thermal resistance, thus enhancing phase-change heat transfer. Besides above metal-based nanomaterials, carbon-based nanomaterials have been used in the BISA process due to the favorable thermal conductivity and chemical stability.[63-65] When 0D self-dispersible GQD was added into nanofluid as working medium for the BISA, a nanoengineered crack-like GQD film was fabricated on the pristine copper (Fig. 3c).[56] This distinct crack-like structure was generated due to the thermal stress between the substrate and GQD film during the BISA. The multi-walled CNTs, as 1D nanomaterial, have been randomly deposited on the copper substrate to form nanoporous structure by the BISA (Fig. 3d).[66] 2D graphene oxide nanosheets were self-assembled layer-by-layer to create ridge-like structure on the substrate (Fig. 3e), while 3D CG particles were stacked densely to generate porous nanostructure

(Fig. 3f).[59, 67]

In addition to films with single surface characteristic by the BISA of individual nanomaterial, films with heterogeneous structures and mixed surface characteristic can be obtained by loading various hybrid nanomaterials for the BISA. Silver/graphene hybrid surface has been formed by loading stable silver/graphene solution as working medium for the BISA (Fig. 3g).[68] It was also demonstrated that graphene connected with functionalized CNT in the solution for the BISA to form a well-ordered porous graphene/CNT hybrid film (Fig. 3h), which showed superior boiling heat transfer capacity than single graphene or CNT film.[69] To achieve mixed surface wettability, hydrophilic GO and hydrophobic CG were combined for the BISA to generate the hybrid GO/CG film (Fig. 3i).[43]

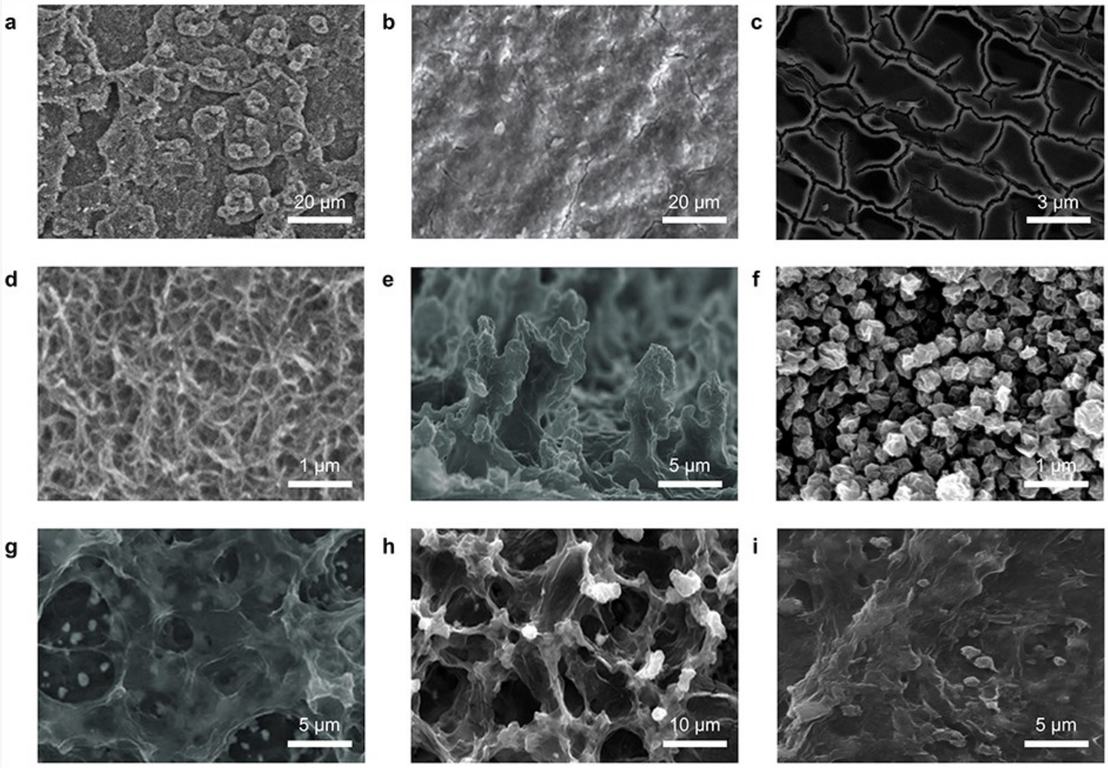

Fig. 3. SEM images of films with nanoengineered surfaces generated by the BISA using various nanomaterials. (a) Alumina nanoparticles. Reproduced with permission.[61] Copyright 2010, Elsevier. (b) Maghemite nanoparticles. Reproduced with permission.[62] Copyright 2017, Elsevier. (c) GQD. Reproduced with permission.[56] Copyright 2023, American Chemical Society. (d) Multi-walled CNTs. Reproduced with permission.[66] Copyright 2020, Elsevier. (e) GO. Reproduced with permission.[67] Copyright 2020, Wiley-VCH. (f) CG. Reproduced with permission.[59] Copyright 2022,

Elsevier. (g) Hybrid silver/graphene. Reproduced with permission.[67] Copyright 2020, Wiley-VCH. (h) Hybrid graphene/CNT. Reproduced with permission.[69] Copyright 2019, Elsevier. (i) Hybrid GO/CG. Reproduced with permission.[43] Copyright 2021, Elsevier.

3.2 Concentration and duration

The concentration of nanofluid containing nanomaterials for the BISA plays a key role in the thickness of the as-fabricated film.[70, 71] The relatively high concentration of nanofluid as the working medium for the BISA enables more nanomaterials to enter the evaporating thin film region and self-assemble to form a dense film on the heated substrate compared to the low concentration of nanofluid (Fig. 4a). It is clearly found that the thickness of films increases with the concentration of nanofluid (Fig. 4b).[59] Although the relationship between film thickness and concentration of nanofluid shows monotonic increase in trend, the excessive concentration leads to the increase of the thermal resistance of generated films, which is adverse to the enhancement of heat transfer.[72] Hence, there exists an optimal concentration of nanofluids for the BISA to generate films with appropriate thickness to effectively dissipate heat and utilize thermal energy.[73]

In addition to the concentration of nanofluid, the self-assembly duration impacts the thickness of generated films. The BISA is a continuous process for self-assembly and deposition of nanomaterials on the substrate when the nanofluid containing enough nanomaterials are used as the working medium (Fig. 4c). With the increase of the duration for the BISA, nanomaterials persistently stack underneath bubbles, and the thickness of generated films increases (Fig. 4d). The appropriate thickness of the films by regulating the self-assembly duration is determined based on the practical applications.[61] Mao et al.[66] found that when the self-assembly duration was less than 40 min, a continuous CNT film cannot be covered completely on the whole substrate, while when the duration further increases, the boiling heat transfer capacity of the generated film has negligible difference. Consequently, considering the efficiency of film generation, an optimized duration for the BISA should be selected.

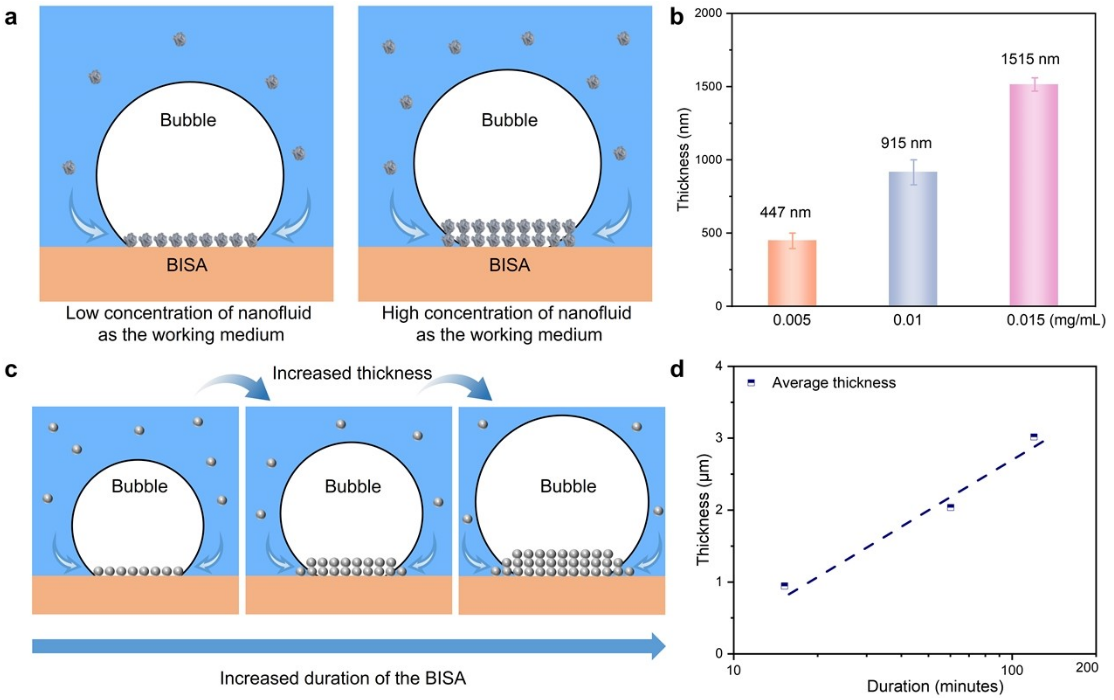

Fig. 4. Film regulation by tuning the concentration of nanofluid containing nanomaterials in the working medium and self-assembly duration during the BISA, respectively. (a) Schematic diagram of films with different thickness by regulating the concentration of nanomaterials in the working medium for the BISA. (b) Relationship between the average thickness and the concentration of nanofluid for the BISA. Reproduced with permission.[59] Copyright 2022, Elsevier. (c) Schematic diagram of films with various thicknesses by regulating the duration of the BISA. (d) Relationship between the average thickness and the self-assembly duration. Reproduced with permission.[61] Copyright 2010, Elsevier.

3.3 Heat flux

The BISA mechanism is mainly related to the bubble dynamic behaviors.[74, 75] The bubble nucleation, growth and departure can be tuned by supplying different heat flux, thus varing the surface micromorphology during the BISA. By controling the applied heat flux, the base graphene layers (BGL) and self-assembled foam-like graphene (SFG) can be generated on the substrate respectively when reduced GO (rGO) nanofluid was used as working medium for the BISA (Fig. 5a).[76] At relatively low heat flux, single bubble nucleation site existed, and rGO nanosheets only horizontally entered the evaporating thin film region under individual bubble due to their larger planar size (several micrometers) compared to the thickness of the evaporting thin film region. Therefore, the rGO nanosheets can self-assemble and densely stack to form the thin BGL. At higher heat flux, more small bubbles emerged on the whole heated substrate and merged. With the assistance of bubbles, SFG were further generated on the BGL by the interaction of hydrogen bonding between nanosheets during the continous BISA (Fig. 5b).

Different heat fluxes at 100, 400, 800 and 1200 kW/m^2 were applied on the heated substrate (Fig. 5c), and under these heat fluxes, the surface morphologies of corresponding generated films were shown in Fig. 5d. At the heat flux of 100 kW/m^2, BGLs with the ring-like lameller structure was generated due to the expansion of the triple-phase line of the bubble. At the input heat flux of 400 kW/m^2, SFG seeds began to form due to bubble coaalescence. With the further increased heat flux, more nucleation sites were activated and bubbles covered the whole heated substrate. Under the condition, the SFG with uniform porosity was generated, and its pore size and thickness could be tuned by varying the input heat flux. In addition, during the BISA, the size of the bubble has an impact on the film structure. For example, Kwark et al.[77] has reported that when the water-based nanofluid was utilized for the BISA, the relativly large bubbles resulted in the non-uniformity of the film due to the high surface tension of water. By comparison, the ethanol-based nanofluid with low surface tension was used, which can produce a quantity of smaller bubbles during the BISA, thus facilitaing the generation of an uniform nanocoating.

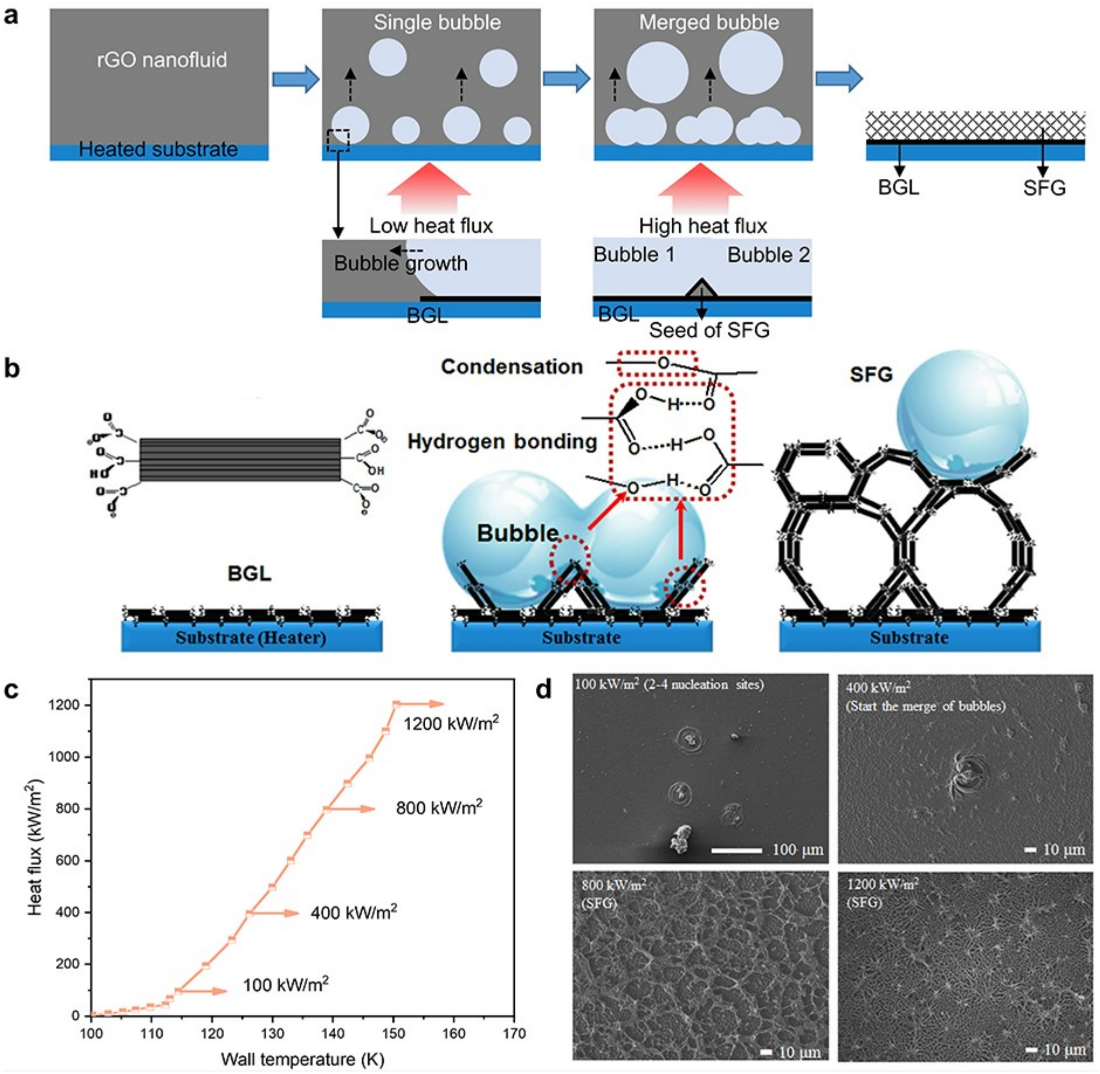

Fig. 5. Film regulation by tuning the input heat flux during the BISA. (a) Schematic diagram of generation process of SFG. (b) Schematic diagram of mechanism of SFG generation. (c) Boiling curve represented by the heat flux and the wall temperature. (d) Various film morphologies by the BISA at different heat fluxes of 100, 400, 800 and 1200 kW/m^2, respectively. Reproduced with permission.[76] Copyright 2013, Springer Nature.

Overall, according to the requirement of desired characteristics of films with nanoengineered surfaces for energy application, suitable nanomaterials can be selected for the BISA. Additionally, films with various surface structures and thickness can be tailored and obtained by simply and reasonably regulating the concentration of nanofluid, self-assembly duration and input heat flux during the BISA.

4. Phase-change heat transfer on films with nanoengineered surfaces by the BISA

Boiling technology, is one of the most efficient ways to utilize and recycle thermal energy by vapor-liquid phase-change process.[78] For the past few years, films with nanoengineered surfaces generated by the simple and low-cost BISA method have been widely applied for boiling heat transfer enhancement.[79-81] Many researches have focused on the design of various surface structures and characteristics based on the enhanced mechanism of boiling heat transfer.[82, 83] A detailed summary about the generated films with nanoengineered surfaces by the BISA of various nanomaterials and their enhancement of boiling heat transfer capacity including CHF and HTC was presented in Table 1.[43, 56, 61, 62, 66-69, 84-88] Boiling process is mainly related to the liquid rewetting and bubble behaviors, such as the bubble nucleation, growth and departure. Several factors that have an impact on boiling heat transfer include the surface wettability, roughness, capillary wicking performance and bubble dynamics (Fig. 6).

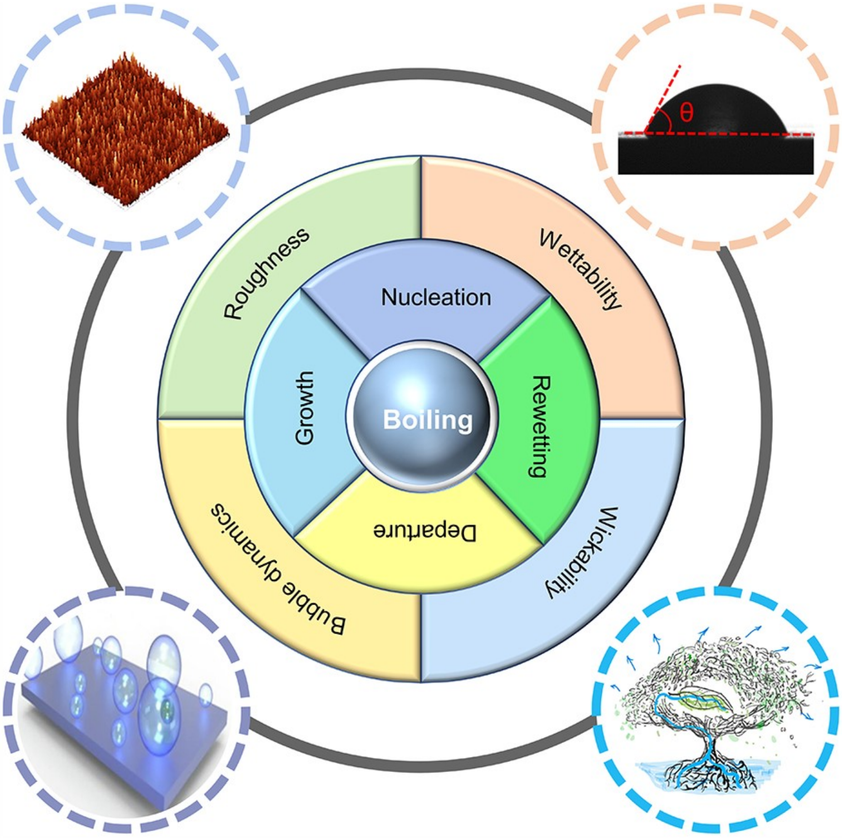

Fig. 6. Overview of factors of boiling-based phase-change heat transfer enhancement.

Due to the significance of the CHF in boiling systems, many theoretical models to predict CHF have been proposed and developed. Table 2 summarized the prevalently accepted modified models according to the original hydrodynamic stability model by taking surface wettability, roughness, and capillary wicking into account, respectively.[89-92] Boiling heat transfer, however, is a very complex process, and accurate prediction of boiling heat transfer capacity needs further exploration. Although the contribution of each factor to the enhancement of boiling heat transfer have not been fully clarified, many studies have considered one or more factors to develop and optimize various structured surfaces by the BISA for enhancing boiling heat transfer. Additionally, we discuss and summarize the studies of films by the BISA on structured surfaces for further boiling enhancement.

Table 1. Summary of researches on boiling heat transfer enhancement for different films with nanoengineered surfaces by the BISA.

Nanomaterial for the BISA	Concentration of nanofluid for the BISA	Surface structure after the BISA	Max CHF (kW/m^2), CHF enhancement	Max HTC (kW/(m^2·K)) , HTC enhancement	Reference
Al_2O_3 nanoparticles	0.025 mg/mL	Alumina nanocoating	1900, 88.1%	/	61
γ-Fe_2O_3 nanoparticles	0.29 mg/mL	Maghemite nanostructure	70, /	10, 66.7%	62
GQD nanofluid	0.001 wt%	Crack-like nanoengineered surface	2439, 169%	107.1, 135%	56
Multi-walled CNT	10 mg/L	Multi-walled CNT nanoporous coating	2177, 86.4%	107, 72.6%	66
Graphene nanofluid	0.0005 wt%	Graphene film	1353, 59%	70, 90%	67
Graphene/silver nitrate nanofluid	0.0005 wt%	Graphene/silver hybrid film	1350, 58.8%	85, 109%	67
Graphene nanoplatelets	0.001 wt%	Graphene nanoplatelets coating	1346, 20%	63, 21%	68

Graphene nanoplatelets-silver hybrid nanofluid	0.003 wt%	Graphene nanoplatelets-silver nanoparticle hybrid coating	1637, 46%	96.9, 82%	68
GO nanofluid	0.005 wt%	GO coated surface	1900, 124%	55, 22%	69
GO/CNT nanofluid	0.005 wt%	3D porous graphene/CNT hybrid coating	2200, 153%	75, 72%	69
GO nanosheets	2 mg/L	Interconnected GO self-assembly surface	2610, 104%	91, 73%	84
Graphene nanoplatelets	/	Graphene nanoplatelets coating	/	280, 582%	85
rGO colloid	0.0005 wt%	3D interconnected foam-like graphene layer	1420, 80%	/, 80%	86
GO solution	0.01 vol.%	Porous graphene surface	228.5, 89.9%	/	87
SiC nanoparticles	0.01 vol.%	Porous SiC surface	195.3, 58%	/	87
Single-walled CNT	0.1 wt%	Porous CNT film	5470, 265%	/	88
GO solution	0.01 mg/mL	GO film with ridge structure	1930, 113%	79.1, 73.5%	43
Hybrid GO/CG solution	0.01 mg/mL	Hybrid GO/CG film with mixed hydrophilic and hydrophobic surface	2270, 150%	120.4, 164%	43

4.1 Surface wettability

Generally, wettability, which is characterized by the static contact angle, is an important factor to determine the boiling heat transfer capacity including the CHF and HTC.[93] The surface with the contact angle less or more than 90° was considered to be hydrophilic or hydrophobic.[94] Hydrophilic surfaces facilitate the rewetting of hot spots during boiling, which benefits for the enhancement of CHF, while hydrophobic surfaces decrease critical activation energy of bubble nucleation, which is favor of the increase of HTC.[95] Despite the tradeoff between wettability and boiling heat transfer capacity, boiling can be divided by applications. The high-heat-flux applications such as electricity generation require more hydrophilic surfaces and higher CHFs, while low-heat-flux applications such as common boilers require relatively hydrophobic surfaces to enable higher HTCs.[96] Surface wettability of films with nanoengineered surfaces can be tuned by loading different nanomaterials with various wettability in the working medium for the BISA. Hydrophilic GO surfaces were developed by the BISA at different self-assembly duration of 2, 2.5 and 4 h, respectively (Fig. 7a).[84] Compared to the pristine copper surface with a contact angle of 88°, GO surfaces showed decreased contact angles due to the hydrophilic oxygen-containing functional groups on GO nanosheets. When GO surfaces were used in a boiling system, it is the favorable wettability of GO surfaces that enables higher CHFs than the pristine copper surface (Fig. 7b). In contrast, hydrophobic surfaces have been generated by employing graphene nanosheets for the BISA to maximize HTC, but the enhancement of CHF was limited.[68]

Table 2. Summary of prediction models for the CHF.

References	Relations	Remarks
Zuber[89]	$q_{CHF} = \frac{\pi}{24}\xi \quad where\ \xi = \sqrt{\rho_l} h_{fg}[\sigma g(\rho_l - \rho_v)]^{\frac{1}{4}}$	Original hydrodynamic instability model
Kandlikar[90]	$q_{CHF} = \frac{1+\cos\alpha}{16}[\frac{2}{\pi}+\frac{\pi}{4}(1+\cos\alpha)\cos\beta]^{\frac{1}{2}}\xi$	Modified hydrodynamic instability model for the effect of wettability
Chu et al.[91]	$q_{CHF} = \frac{1+\cos\alpha}{16}[\frac{2(1+R_a\cos\theta_r)}{\pi(1+\cos\alpha)}+\frac{\pi}{4}(1+\cos\alpha)\cos\beta]^{\frac{1}{2}}\xi$	Hydrodynamic instability model considering surface roughness
Wen et al.[92]	$q_{CHF} = \frac{1+\cos\alpha}{16}[\frac{2}{\pi}+\frac{\pi}{4}(1+\cos\alpha)\cos\beta]^{\frac{1}{2}}\xi + \frac{\rho_l h_{fg}}{A_b}V_w$	CHF model considering the capillary wicking

In order to address the tradeoff between CHF and HTC and simultaneously enhance the CHF and HTC, film surfaces with mixed hydrophilic and hydrophobic characteristics was developed by the BISA when the hybrid GO/CG solution was used as working medium.[43] To avoid the thermal reduction and agglomeration of GO nanosheets dispersed in the hybrid solution at relatively high temperature, the self-assembly temperature was controlled at 60 °C. On the hybrid GO/CG film, hydrophilic GO parts mainly contributed to the wetting of liquid and provided liquid supplementary into the evaporating thin film region underneath bubbles during boiling, and hydrophobic CG particles lowered nucleation energy of bubbles and provided a quantity of bubble nucleation sites (Fig. 7c). Comparing to the single wettability of GO film and CG film, the mixed wettability of the developed hybrid GO/CG film achieved the separation of vapor-liquid pathway, which enabled both high CHF and HTC.

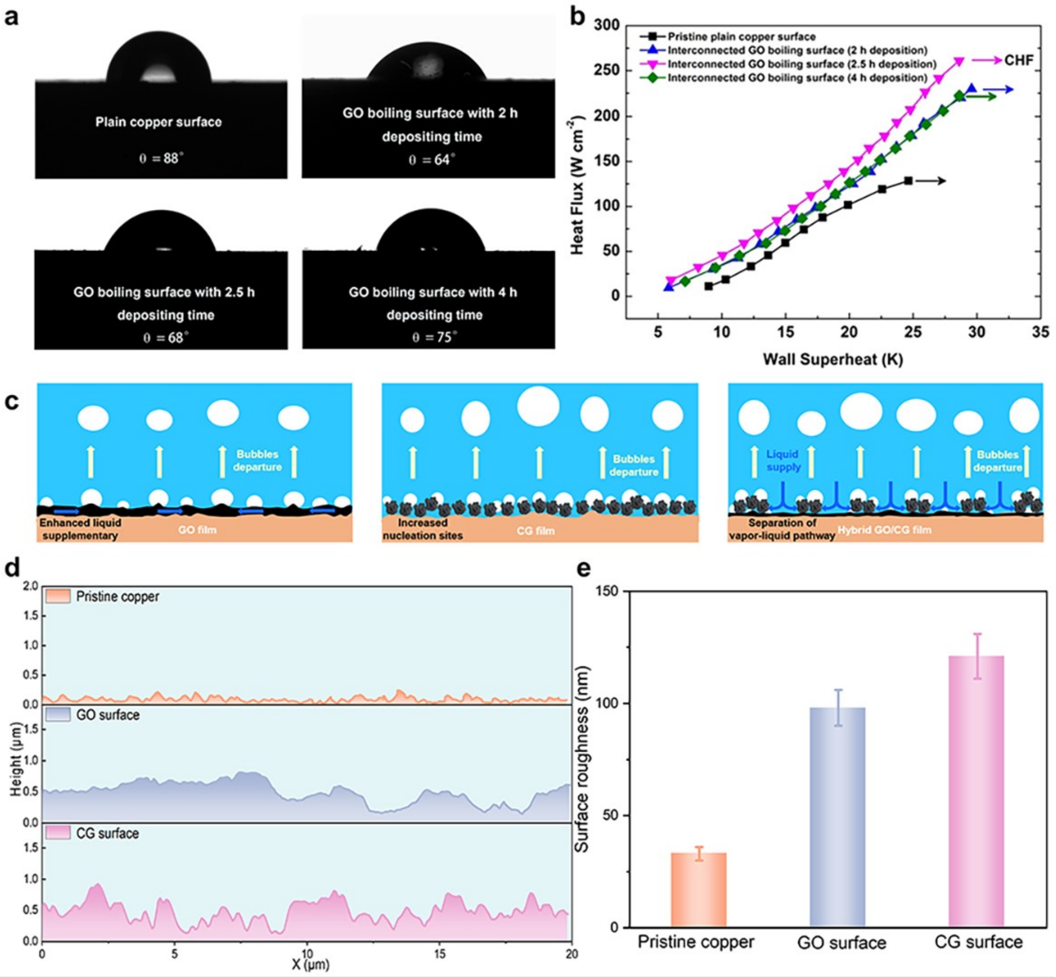

Fig. 7. Surface wettability and roughness of the films with nanoengineered surfaces by the BISA. (a) Contact angles of the pristine copper and GO surfaces generated by the BISA. (b) Corresponding

boiling curves of the surfaces in (a). Reproduced with permission.[84] Copyright 2019, Elsevier. (c) Schematic diagram of bubble growth on the GO film, CG film and hybrid GO/CG film, respectively. Reproduced with permission.[43] Copyright 2021, Elsevier. (d) Height profiles of the pristine copper, GO film, and CG film based on the AFM images, respectively. (e) Corresponding surface roughness according to the topographic images of surfaces in (d) measured by AFM. Reproduced with permission.[59] Copyright 2022, Elsevier.

4.2 Surface roughness

Surface roughness is another key factor to influence the CHF and HTC.[97] Furthermore, it is closely related to the surface wettability, nucleation sites of bubbles, and surface area of heat transfer during boiling.[98] After the BISA of alumina nanofluid, a heterogeneous coating was rapidly generated on the smooth aluminum substrate, which roughened the surface.[99] The larger the concentration of nanofluid for the BISA was, the rougher the coating surface became after BISA. Meanwhile, the contact angle of the coating surface decreased compared to the original substrate, which was consistent with the theory that the hydrophilicity of hydrophilic surface was better with the increased roughness.[100]

The enhanced CHF and HTC were achieved on the CG surface by the BISA compared to the pristine copper and GO surface.[59] The enhancement is mainly due to the nanostructure and increase of surface roughness. The pristine copper is relatively smooth, but the self-assembled CG surface has peaks and valleys due to the wrinkled morphology on CG particles (Fig. 7d). According to the micromorphology characterization by atomic force microscopy (AFM), the pristine copper and GO surface showed average surface roughness of 33 and 98 nm, respectively, while CG surface presented the increased surface roughness of 121 nm (Fig. 7e). The CG surface with maximum surface roughness among above surfaces provided a quantity of bubble nucleation sites, which was responsible for the enhancement of CHF and HTC.

Most studies have reported the increased surface roughness after the BISA of nanomaterials, but a few of researchers found the opposite results. It should be noted that the surface roughness actually can increase or decrease after the BISA, which depends on the condition of the original substrate and the size of nanomaterials for the BISA.[101] When the roughness of the original substrate was smaller than the size of nanomaterial, the roughness of the modified surface after the BISA increased. On the contrary, if the roughness of original substrate was larger than the size of nanomaterials, the surface roughness after the BISA was able to decrease. Despite the decreased surface roughness, its boiling CHF and HTC can be likely to be improved. It was mainly due to the increase of surface area for heat transfer by splitting large cavities on the rough original substrate into several small cavities after the BISA of nanomaterials.[102]

4.3 Capillary wicking

Besides the surface wettability and roughness, capillary wicking performance has been considered as an important indicator to affect the boiling CHF and HTC.[103] Water-based nanofluid containing TiO_2 nanoparticles was employed for the BISA to self-assemble and form a porous nanocoating on the substrate, which caused a significant improvement of CHF.[104] Different porous surfaces with various contact angles ranging from 70° to 20° were generated by using nanofluids with the volume concentration from 10^{-5}% to 10^{-1}%, respectively. The generated surfaces both showed a contact angle of 20° when the volume concentration of nanofluids for the BISA were 10^{-3}% and 10^{-1}%. There existed an interesting phenomenon that at the same contact angle, the experimental CHF of the surfaces generated by the BISA, however, further increased from 1500 kW/m^2 to 2500 kW/m^2. The wettability alone cannot explain such enhancement of CHF, and the capillary wicking on the nanocoated surface by the BISA, which depicted the dynamic wetting and wicking of liquid, should also be considered (Fig. 8a). The capillary wicking performance of above two surfaces was characterized by the capillary liquid rise height with 0.9 mm and 5.5 mm, respectively. It was concluded that the self-assembled porous layer not only changed the wettability of the original substrate, but also resulted in the high capillary wicking performance, which facilitated the rewetting of local hot spots and delayed the occurrence of CHF.

By using Al_2O_3 nanoparticles for the BISA, the obtained nanocoated surfaces enhanced CHF.[105] The enhancement mechanism was ascribed to the favorable wettability and capillary wicking performance. To characterize the wicking behavior, a vertical dipping experiment was performed on the optimal nanocoated surface, which was generated by the BISA with the duration for 5 min. According to the high-speed images after dipping at different time, the liquid meniscus finally rose from the horizontal plane to about 2.6 mm onto the nanocoated surface (Fig. 8b). In addition to the maximum capillary rise height, a relatively high wicking speed on the nanocoated surface enabled efficient rewetting of hot spots underneath boiling bubbles and thus helped improve the CHF.

A self-assembly nanoporous CNT surface with high stability and durability has also been developed by using the simple and low-cost BISA strategy.[66] This nanoporous CNT surface, which was used in a boiling system, showed the enhancement ratios of the CHF and HTC up to 86.4% and 72.6% compared to the pristine copper, respectively. It was found that hydrophilic characteristic and high-performance capillary wicking of the nanoporous CNT surface benefited for the liquid circulation at triple-phase interfaces and prevented the vapor film from covering the whole surface during boiling. According to the paragraphs captured by the infrared thermal imaging camera, no capillary wicking height was observed on the pristine copper, while a distinct capillary wicking height was shown on the nanoporous CNT surface (Fig. 8c and 8d). Consequently, a good capillary wicking performance on the nanoporous CNT surface enabled enough liquid supplementary under boiling bubbles and thus enhanced the CHF and HTC. Besides above testing methods, droplet spreading experiment can be performed to characterize the capillary wicking performance. Compared to the pristine copper and GO film (Fig. 8e and 8f), the GQD film generated by the BISA had higher capillary wicking performance due to the enhanced dynamic wetting in addition to the improved static wetting (Fig. 8g). This enhanced dynamic wetting was due to the larger internal spacing and lower flow resistance of crack-like nanostructure on the GQD film.[56]

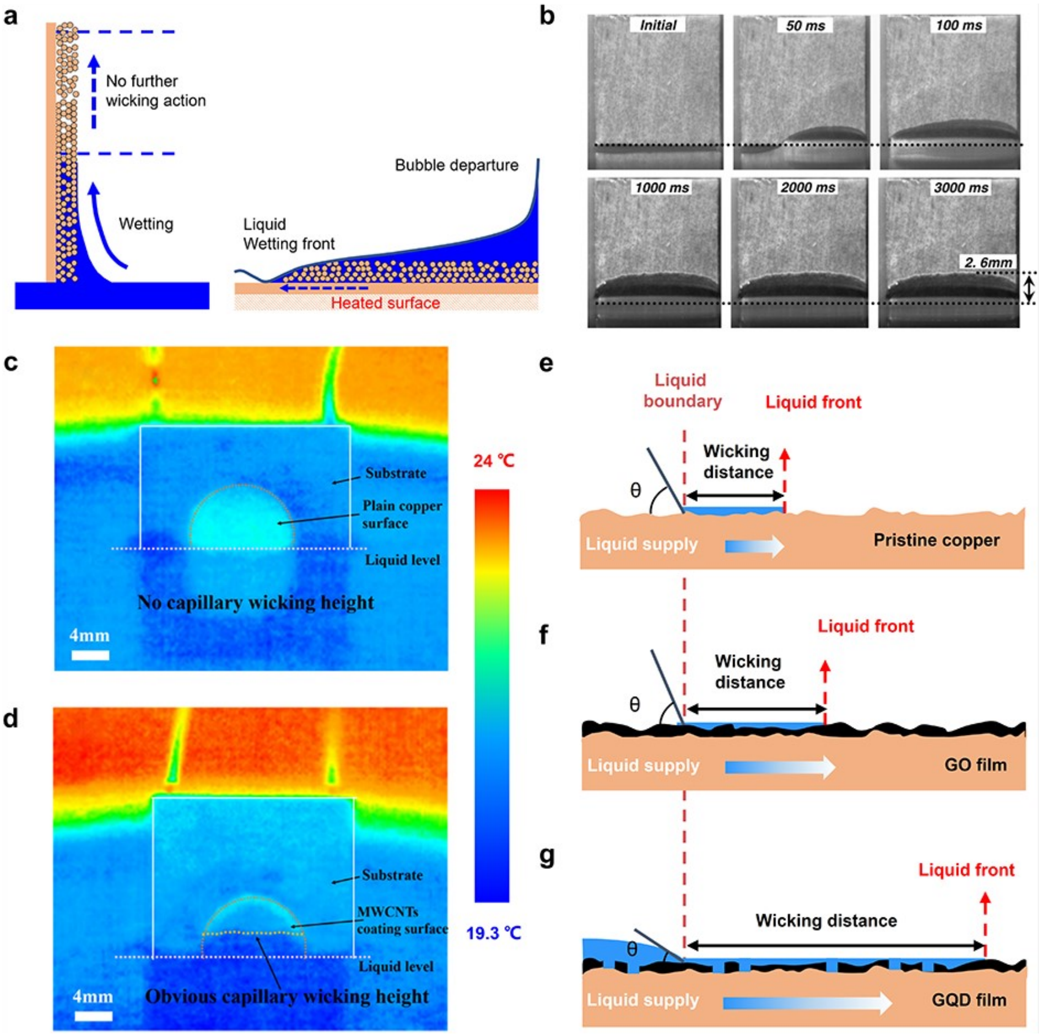

Fig. 8. Capillary wicking performance on films with nanoengineered surfaces by the BISA. (a) Wetting and wicking mechanism of the nanocoated surface by the BISA. (b) Capillary wicking on the nanocoated surface. Reproduced with permission.[61] Copyright 2010, Elsevier. Capillary wicking performance of (c) plain copper surface and (d) CNTs nanoporous coating surface measured by infrared thermal imaging camera. Reproduced with permission.[66] Copyright 2020, Elsevier. Static wetting (contact angle) and dynamic wetting (capillary wicking) of deionized (DI) water on (e) pristine copper, (f) GO film, and (g) GQD film, respectively.

4.4 Bubble dynamics

In general, bubble dynamics, which consists of bubble nucleation, growth and departure, is of importance to determine the boiling CHF and HTC.[106] The CHF and HTC of the GO nanocoating surface, which was fabricated by the BISA of GO nanosheets, were 78% higher and 128% higher compared to the pristine copper, respectively.[107] It was mainly due to the fact that the GO nanocoating surface not only showed a hydrophilic characteristic, but also provided many nucleation sites of bubbles. The observation of the bubble dynamics during boiling could gain a detailed comprehension of the enhanced boiling heat transfer capacity. The high-speed images showed the bubble coalescence on the pristine copper and GO nanocoating at low heat fluxes of 20, 50 and 80 kW/m^2, respectively (Fig. 9a and 9b). At the same applied heat flux, it was obvious that bubbles were prone to merge and form bubble column on the pristine copper over the GO nanocoating surface, which delayed the occurrence of film boiling and resulted in a higher CHF. Meanwhile, by comparison with the pristine copper, the bubble departure diameter was smaller and departure frequency was faster on the GO nanocoating surface at similar heat fluxes, thus contributing to the heat dissipation by vapor-liquid phase change and improving the boiling HTC.

The bubble dynamics on the GO film with ridge-like structure and the GQD film with crack-like structure was further studied and quantitatively analyzed (Fig. 9c-e).[56] The bubble departure diameter of the GQD film with the distinct crack-like nanostructure was smaller compared to the pristine copper and GO film (Fig. 9c). It is the favorable wettability of the GQD film that decreased the surface tension, which resulted in small bubble departure diameter. Commonly, the bubble departure diameter was inversely proportional to the departure frequency. Thus, the GQD film had the lowest bubble departure frequency among surfaces (Fig. 9d). With the increase of the heat flux, more bubble nucleation cavities are activated. The bubble nucleation site density of the GQD film with crack-like structure was nearly triple than that of the pristine copper (Fig. 9e). The small bubble departure diameter, high departure frequency and abundant nucleation sites on the GQD film during boiling enabled efficient thermal energy management.

To summarize, based on fundamental factors affecting phase-change heat transfer, we can rationally control surface characteristics of films with nanoengineered surfaces by loading nanomaterials with different properties in the working medium for the BISA to effectively utilize thermal energy.

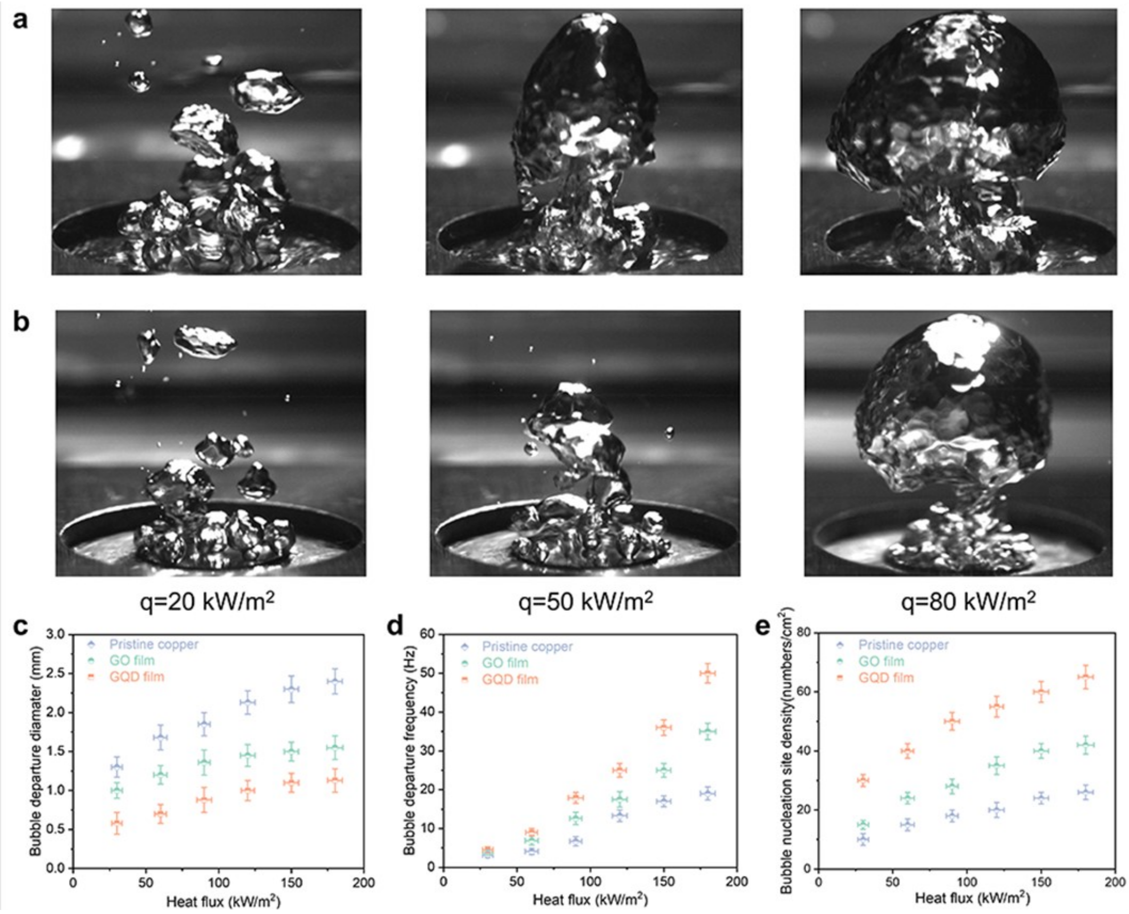

Fig. 9. Bubble dynamics on film surfaces via the BISA. Bubble nucleation, growth and departure obtained by the high-speed camera on (a) pristine copper and (b) GO nanocoating surface during boiling at the low heat flux regime of 20, 50 and 80 kW/m^2, respectively. Reproduced with permission.[107] Copyright 2020, Elsevier. Parameters of bubble dynamics including (c) bubble departure diameter, (d) bubble departure frequency and (e) bubble nucleation sites on the pristine copper, GO film and GQD film as a function of heat flux, respectively. Reproduced with permission.[56] Copyright 2023, American Chemical Society.

4.5 Further boiling enhancement of films on structured surfaces by the BISA

The film surfaces can not only be generated on the pristine smooth substrate, but also combine with structured surfaces by the BISA strategy for further enhancing boiling heat transfer. The nanoparticle coated (NPC) surface and hybrid micro/nanoscale modulated porous coating (HMPC) surface by the BISA of copper oxide nanoparticles were prepared on the bare metal surface and modulated microscale porous (MMPC) surface, respectively (Fig. 10a).[108] The original MMPC surface was fabricated by the hot powder compaction of copper powders with an average diameter of 200 μm. This study have reported the unexpected conclusion that the values of both boiling CHF and HTC of the HMPC surface were not larger than those of the MMPC surface. This is mainly due to the uniform and dense deposition and coverage of nanoparticles on the original MMPC surface by the BISA, which blocked the bubble nucleation sites and increased the thermal resistance for heat transfer on the HMPC surface.[109] An rGO-coated micropillar surface (GMS) was proposed to enhance nucleate boiling heat transfer.[110] The micropillar surface was fabricated by using the MEMS procedure (Fig. 10b), and the rGO porous layer was further coated on the top of the micropillar surface by the BISA of rGO solution with the concentration of 0.0005 wt% (Fig. 10c). The porous rGO structure mainly provided considerable bubble nucleation sites, while the micropillar structure, which had favorable capillary wicking performance, facilitated the liquid supply to vapor bubbles and thus avoided the coverage of the vapor film on the whole heating surface during boiling. Consequently, the separation of the vapor-liquid pathway was achieved on the GMS in order to synergistically increase the CHF and HTC up to 152% and 288% over the pristine surface, respectively.

A patterned surface with rGO-coated micropillar-free cavities was further designed to suppress bubble coalescence for enhancing boiling heat transfer.[111] The patterned surface was generated by two steps (Fig. 10d). The micropillar surface with cavity was generated by photolithography and deep reactive ion etching, and subsequently a sectored BISA method was used to fabricate the rGO coated surface on the micropillar surface with artificial cavities. Additionally, the rGO coating fabrication can be regulated by different heat flux during the BISA (Fig. 10e). The morphology of the patterned surface demonstrated a porous coating on the micropillars and a thin film on the cavity. The patterned surface with rGO-coated micropillar-free cavities not only provided enough nucleation sites for bubbles, but also enabled the liquid supply through rGO porous layer and allowed liquid flow between the micropillars. Hence, bubble merge was reduced, and occurrence of vapor film was delayed. A nanoparticle-deposited honeycomb porous plate have also been prepared to effectively enhance the boiling CHF.[112] The enhancement is mainly due to the improved capillary wicking performance for liquid supplementary during boiling. The finding also revealed the considerable improvement of CHF on the modified heated surface with a diameter of 30 mm by the nanoparticle deposition via the BISA, which was promising for the application of heat dissipation on large-area surfaces.

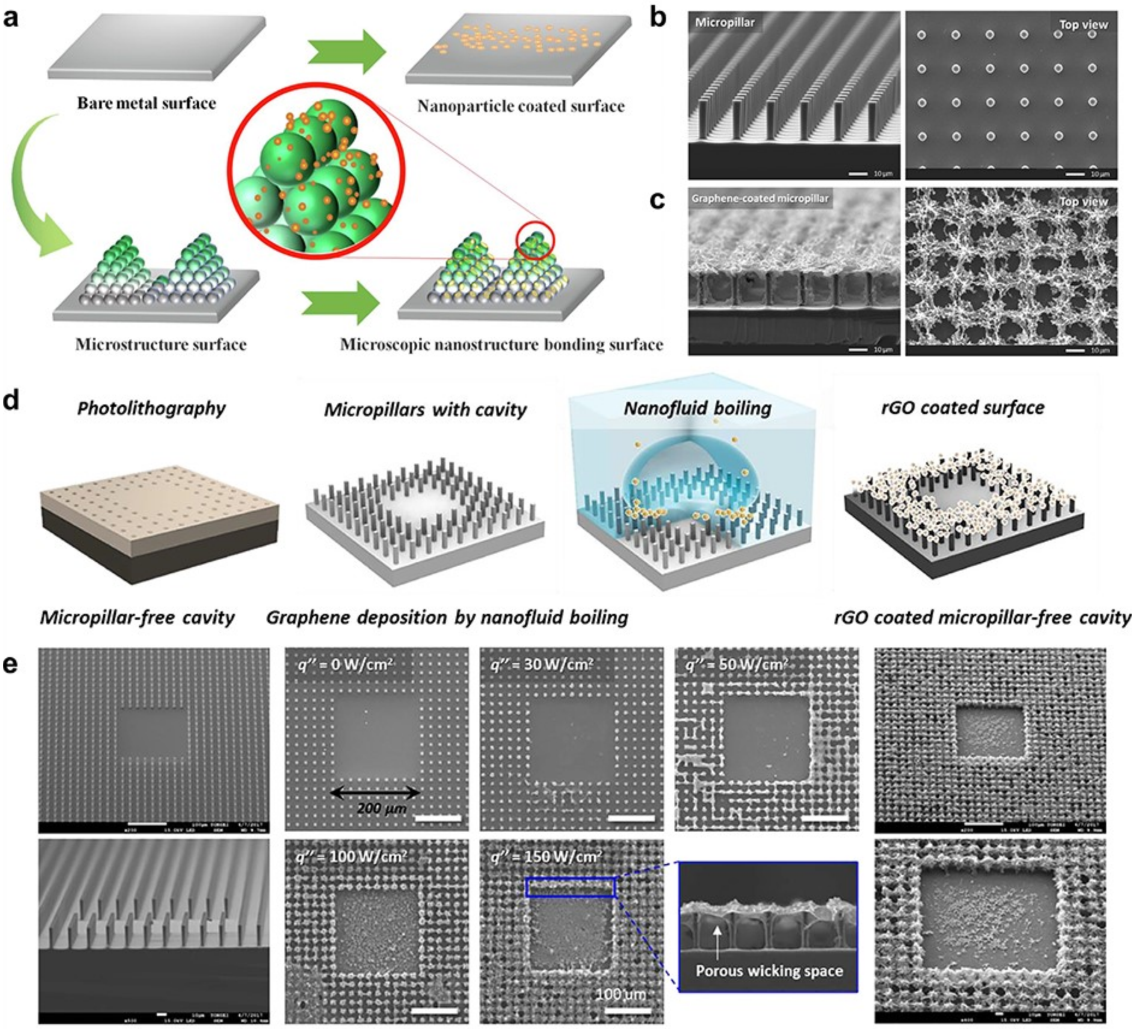

Fig. 10. Films with nanoengineered surfaces generated on structured surfaces by the BISA. (a) Schematic diagram of nanoparticle deposition by the BISA on the pristine smooth surface and microstructure surface, respectively. Reproduced with permission.[109] Copyright 2022, Elsevier. The lateral view and top view of (b) micropillar surface and (c) graphene-coated micropillar surface. Reproduced with permission.[110] Copyright 2019, Elsevier. (d) Generation process of rGO coated micropillar surface. (e) SEM images showing the deposition process of rGO sheets on the micropillar surface. Reproduced with permission.[111] Copyright 2022, Elsevier.

5. Emerging advanced methods for the BISA

Above description mainly concentrates on the BISA strategy based on the microlayer evaporation underneath bubbles during boiling. Recently, some new researches have begun to focus on advanced methods for the BISA to generate films with different nanoengineered surfaces. In this section, we mainly highlight two emerging strategies for the BISA including the laser-generated BISA and BISA at the air-liquid interface.

5.1 BISA via the femtosecond laser

Bubbles can be generated not only by phase-change process, but also by laser-induced photothermal effect. Generally, the size of generated bubbles by phase change is tens of microns, while the bubbles by femtosecond laser reach several micrometers or less.[113] When the laser with the wavelength of 532 nm focused on the plasmonic substrate such as gold film, a microbubble was formed at the solid-liquid interface, and its size can be varied with the minimum size of 1 μm by tuning the intensity of laser (Fig. 11a).[114] Rapid evaporation underneath the microbubble induced the Marangoni convection and capillary flow to replenish liquid containing polystyrene (PS) nanoparticles towards the microbubble. Thus, PS nanoparticles with the size of 540 nm can self-assemble and deposit on the substrate under the microbubble. By precisely steering the laser beam, the microbubble can move by the designed trajectories to obtain various desired nanostructures. Despite the patterning PS nanoparticles, the BISA strategy by femtosecond laser also demonstrated the feasibility of controlling the self-assembly of fluorescent quantum dots with the size of 6 nm, showing considerable potential for the application of optoelectronic devices (Fig. 11b).[115]

In addition to the occurrence of laser-generated BISA on the plasmonic substrate, the BISA process can happen when microbubbles are directly generated on the laser-absorbing particles.[116] The self-assembly and deposition mechanism of the BISA of laser-absorbing particles, however, is different. The plasmonic metal nanoparticles were activated to generate microbubbles and boost the growth under the irradiation of femtosecond laser.[117] Due to the existence of metal nanoparticles in the irradiation region of laser, temperature increases over the microbubble and direction of induced capillary flow is towards the microbubble (Fig. 11c).[118] This capillary flow finally carried the suspended nanoparticles in the solution to the triple-phase contact line (TPCL) of the microbubble, and nanoparticles were self-assembled and immobilized on the substrate with the microlayer evaporation at the TPCL by laser heating (Fig. 11d). With the laser moving, the self-assembled nanoparticles were acted as a new local heat source to generate another bubble and thus caused bubble movement with the direction of laser to generate continuous self-assembly of nanoparticles.[119]

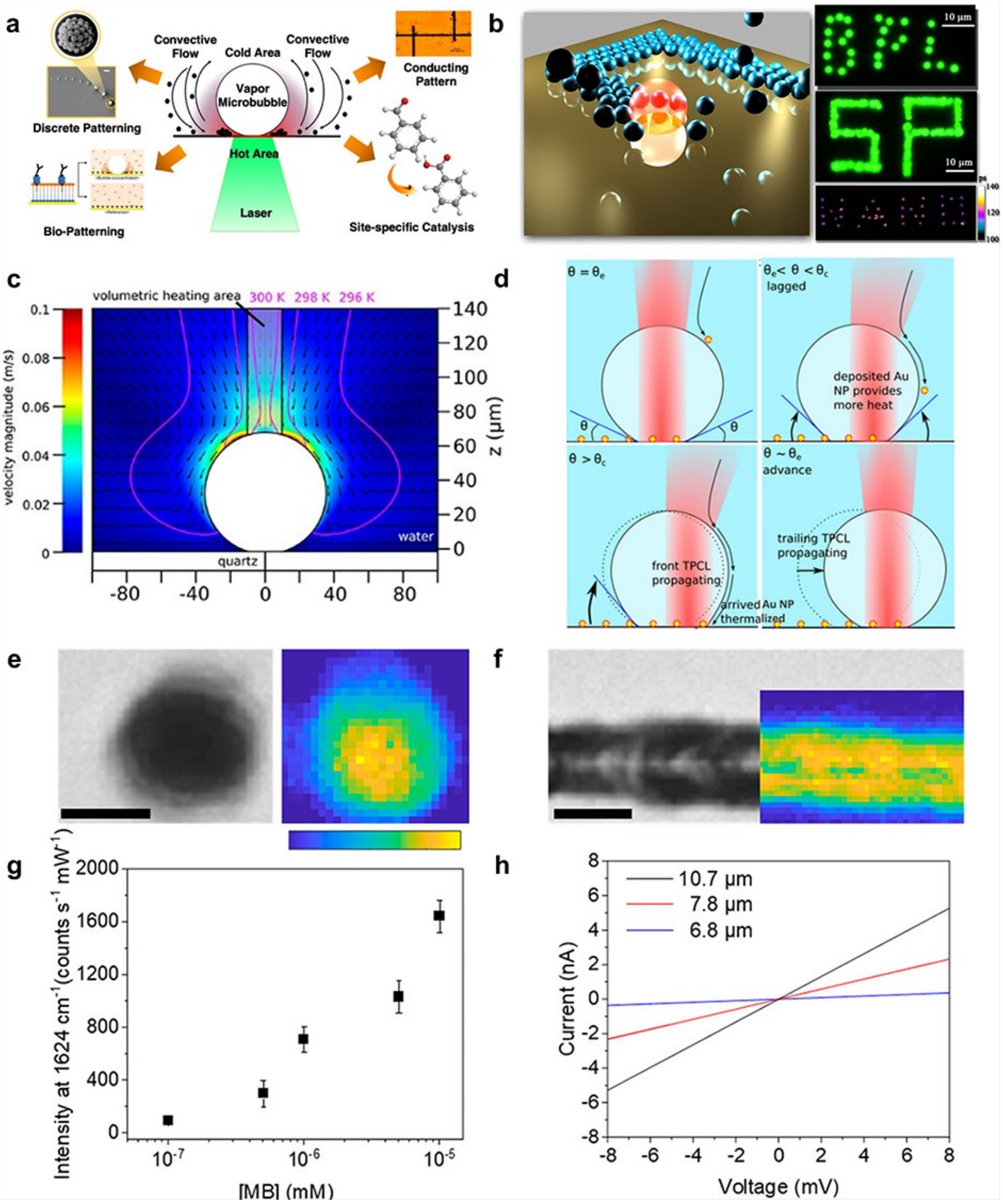

Fig. 11. BISA via the femtosecond laser. (a) BISA mechanism on femtosecond laser-absorbing substrates to generate nanoengineered surfaces and their diverse applications. Reproduced with permission.[114] Copyright 2021, American Chemical Society. (b) BISA of PS nanoparticles and quantum dots on gold film due to the plasmonic photothermal effect. Reproduced with permission.[115] Copyright 2016, American Chemical Society. (c) Simulated capillary flow around individual bubble after the irradiation of femtosecond laser on laser-absorbing particles. (d) BISA mechanism of laser-absorbing particles. Reproduced with permission.[118] Copyright 2019, American Chemical Society. SERS mapping of the MXene (e) lines and (f) points via the BISA. Black scale

bar is 5 μm, and color scale ranges from 0 to 12000 counts. SERS performance of MXene patterned nanostructures. (g) Mean SERS intensity of MXene patterns at different concentration of methylene blue. Conductive property of MXene lines by the BISA. (h) I-V curves of generated MXene lines with different width. Reproduced with permission.[120] Copyright 2023, American Chemical Society.

Besides the metal-based nanoparticles, recently some 2D nanomaterials with plasmonic property can be applied for the laser-generated BISA. To directly generate microbubbles and deposit the nanomaterials by the femtosecond laser without the prior fabrication of the plasmonic substrate, MXene nanosheets was dispersed in solution as the working medium for the BISA.[120] MXene can also absorb laser beam to generate heat for microbubble formation. With the movement of the substrate, MXene nanosheets can be deposited and patterned on the substrate by the BISA. The generated MXene nanostructures showed favorable plasmonic property, which demonstrated an essentially consistent signal whether line pattern or dot pattern by surface-enhanced Raman scattering (SERS) spectrum (Fig. 11e and 11f). With the increased concentration of MXene nanosheets in the solution for the BISA, the SERS signal of the generated MXene patterns was enhanced (Fig. 11g). Moreover, the self-assembled MXene patterns by the BISA also showed conductive property according to the I-V curves, which offers a different strategy for fabricating electronic circuits (Fig. 11h).

In conclusion, the strategy of the BISA by femtosecond laser is suitable for the generation of large-scale patterned surfaces with desirable properties on arbitrary substrates, which demonstrates the feasibility of the strategy in practical applications.

5.2 BISA at the air-liquid interface

Aside from the generation of films with nanoengineered surfaces on the solid substrate by the BISA, films can be generated at the air-liquid interface.[121] When the GO/exfoliated graphene (GO/EG) nanofluid was heated at a relatively mild temperature below 80 °C, a self-assembled laminated GO/EG film was generated due to the evaporation of the nanofluid (Fig. 12a). When the heated temperature reached over the boiling point of the nanofluid, however, violent bubbles rose, and broke the superficial self-assembled film at the air-liquid interface. Under the capillary force, the GO/EG nanosheets aggregated and crumpled into microspheres (Fig. 12b). Compared to the laminated film, the microsphere graphene shorted the pathway of ion transportation, which enabled high ion conductivity and showed promising in the application of supercapacitors (Fig. 12c).[122]

Furthermore, a large-scale freestanding microsphere film with length of 1.2 m, which consisted of GO/EG microsphere, can be rapidly generated by a facile roll-by-roll process (Fig. 12d). When the microsphere film is used as an electrode of supercapacitor, the cyclic voltammetry (CV) curve of microsphere film demonstrated superior capacitive performance compared to the laminated film (Fig. 12e). The generated flexible supercapacitor showed favorable bending stability with 97.6% of the original capacitance after 5000 cycles of bending, and were able to lighten 72 red LEDs (Fig. 12f). This microsphere film as electrodes generated by the BISA exhibited high potential utilization in supercapacitors to provide power for flexible electronics. Due to the universality of boiling bubble rising, in addition to graphene-based materials, the BISA strategy at the air-liquid interface can be suitable to fabricating microspheres of other 2D nanomaterials including MXene, boron nitride (BN) and transition metal dichalcogenides (TMDs).

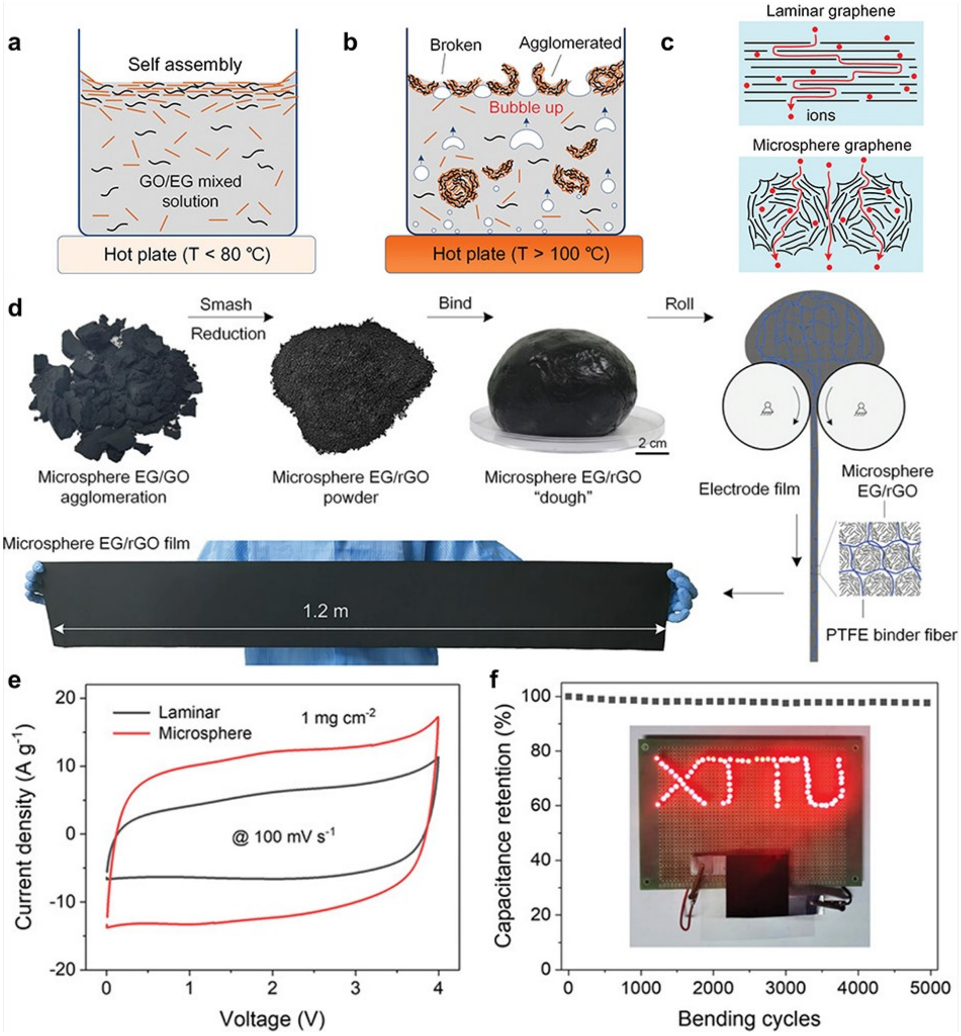

Fig. 12. BISA at the air-liquid interface. (a) Laminated film generated by the evaporation-induced self-assembly. (b) Microsphere graphene generated by the BISA at air-liquid interface. (c) Ion transportation in the laminated graphene film and microsphere graphene, respectively. (d) Generation procedure of large-scale microsphere graphene film. (e) CV curves of laminated graphene film and microsphere graphene film. (f) Capacitance retention of flexible solid-state supercapacitors when microsphere graphene films are used as symmetric electrodes. Inset: photography of 72 LEDs lightened by the flexible solid-state supercapacitor. Reproduced with permission.[121] Copyright 2023, Wiley-VCH.

Overall, the universal BISA strategy not only can achieve the self-assembly of nanomaterials to form films with nanoengineered surfaces underneath bubbles during pool boiling, but also use some advanced methods to generate films, such as using laser-induced photothermal bubbles to self-assemble and heating nanofluids to generate boiling bubbles for the self-assembly at the air-liquid interface.

6. Diverse energy applications of films with nanoengineered surfaces by the BISA

The BISA strategy has been widely used to develop high-performance films with nanoengineered surfaces for heat-related applications. Recently, many researchers have employed and carried forward this strategy to generate films for diverse energy-related applications. In this section, we focus on prominent energy applications of the BISA including light emitting dioxide (LED), photovoltaic cells, gas and liquid sensors, and catalysis.

6.1 BISA for LED and photovoltaic cells

Recent years have witnessed rapid development in utilizing the films with nanoengineered surfaces by the BISA for efficient thermal energy management of high-power devices. By suitable thermal management, energy devices can improve the operation lifespan and efficiency, which contributes to energy conservation and emission reduction. Based on the BISA method, a porous superhydrophilic surface coated with graphene nanoplatelets (GNP) has been fabricated for thermal management of LED.[85] It is generally recognized that the lifespan of electronics is related to the working temperature, which follows the rule of thumb that a 10 °C increase of working temperature results in the decrease of lifespan by 50%. When the power input reached 36 W, the junction temperature of LED by phase-change thermal management on the uncured GNP and cured GNP were decreased by 9.1 °C and 15.5 °C, compared to the uncoated surface based on the temperature profile measured by infrared camera (Fig. 13a). Under the circumstance, according to the Arrhenius model, the lifespan of LEDs cooled by the uncured GNP and cured GNP have correspondingly prolonged by 1.9 times and 2.9 times over that cooled by uncoated surface, respectively.

Effective thermal management for concentrated photovoltaics (CPV) places an increased emphasis on the generation of high-performance surfaces, which enables sustainable energy utilization. Boiling heat transfer has been widely applied for the thermal management of the CPV due to its capability to effectively dissipate high heat flux.[123] A 3D graphene/silver hybrid film with porous structure was developed by the BISA for the thermal management of CPV system (Fig. 13b).[67] It is necessary to increase the overall production of the CPV system by concentrating more solar energy on CPV cells. Heat flux and temperature, however, increase rapidly, thus decreasing the cell efficiency and even damaging the cell in the high-temperature condition.[124] The enhanced boiling heat transfer capacity allows the CPV system to withstand high heat flux and increase the production without sacrificing the cell efficiency. The electricity and steam generation of the CPV system using the graphene/silver hybrid film were evaluated as 60.8 and 119.4 MW, which increased by 48 and 94.2 MW over those of the CPV system using the plain surface. In addition, GQD films on micropillar (MP) surface and copper powder-sintered (CP) surface generated by the BISA were used for thermal energy management of CPV system, respectively (Fig. 13c).[56] The electrical efficiency of the CPV cell, which was integrated with MP-GQD film surface and CP-GQD film surface, achieved 36.62% and 36.61% in comparison to the pristine copper (35.95%).

The BISA strategy can not only generate 2D graphene-based films for efficient thermal energy management, but also form 3D films as the counter electrode for solar cells. A self-assembled foam-like graphene (SFG) film was fabricated by the BISA, which was governed by the nucleation and departure of bubbles in the graphene nanofluid during the BISA.[76] The SFG film can be generated on various substrates, such as metals, glasses and polymers. The thermal conductivity and resistance of the SFG film reached 11.8 $S\cdot cm^{-1}$ and 91.2 Ω^{-1}, respectively, which were equivalent to those of the graphene film prepared by CVD method. Due to the large surface area and favorable capability for charge delivery, the SFG film with porous structure was generated on the fluorine-doped tine oxide (FTO) by the BISA as the cathode of quantum dot sensitized solar cells (QDSSCs) (Fig. 13d).

The SFG film showed the photovoltaic performance with an overall cell efficiency of 3.6%, which was better than the commercial state-of-art gold electrode (Fig. 13e).

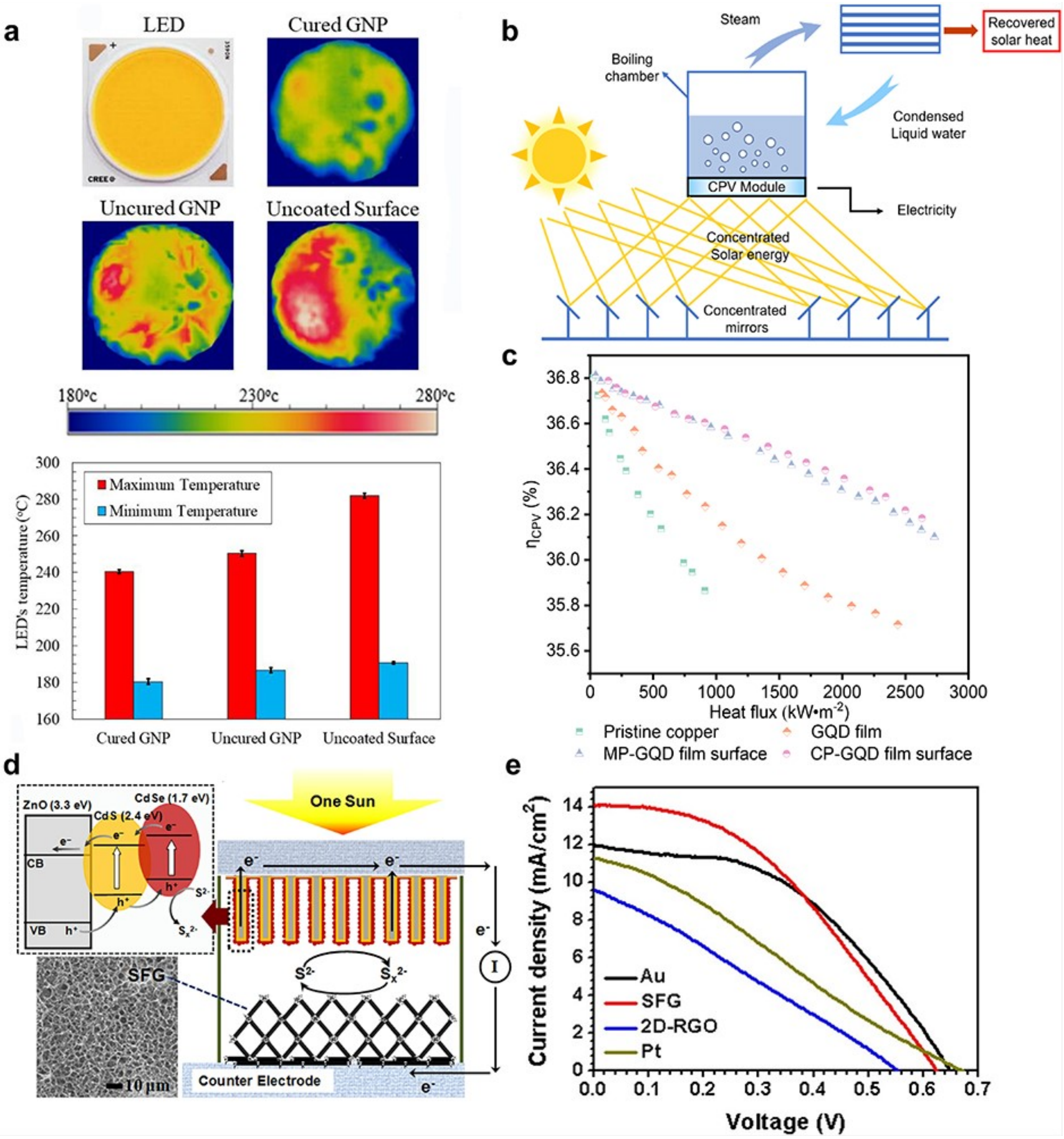

Fig. 13. BISA for LED and photovoltaic cells. Enhanced LED cooling performance. (a) Temperature distribution of LED cooled by subcooled boiling on the cured GNP, uncured GNP and uncoated surface. Efficient thermal management of CPV system. Reproduced with permission.[85] Copyright 2021, Elsevier. (b) Integration between CPV and thermal management system based on boiling. (c) Comparison of electrical efficiency of CPV cell when the pristine copper, GQD film, MP-GQD film surface, and CP-GQD film surface are used as boiling substrates, respectively. Reproduced with permission.[56] Copyright 2023, American Chemical Society. Enhanced overall

efficiency of QDSSCs. (d) Self-assembled foam-like graphene-based QDSSCs. (e) Performance of QDSSCs when SFG is used as the counter electrode. Reproduced with permission.[76] Copyright 2013, Springer Nature.

6.2 BISA for gas and liquid sensors

Hydrogen is currently an alternative and clean energy compared to conventional fossil fuel due to its high energy density, which has broad application perspective.[125] Hydrogen, however, is colorless, tasteless and flammable.[126] To ensure reliable utilization of hydrogen, accurate detection of generation and leakage of hydrogen is quite necessary. Palladium is a widely used material for hydrogen sensors by dissociative absorption.[127] General generation of hydrogen sensors require two procedures including the fabrication of palladium crystals and then the deposition of them into desired structures. The laser-generated BISA can achieve one-step generation of palladium-based hydrogen sensors on the target substrate (Fig. 14a).[128] A hydrogen sensor was directly fabricated by the BISA of palladium/nickel nanoparticles on the gold substrate (Fig. 14b). The sensing mechanism is due to the relative resistance change when hydrogen is absorbed on the self-assembled palladium/nickel structure. The generated hydrogen sensor by the BISA can detect the minimum concentration of hydrogen up to 100 ppm in air (Fig. 14c).

A smart superhydrophobic polypropylene (PP)/open-cell graphene network (OGCN) with sensing ability for droplets has been designed by the facile and economical boiling method.[129] The PP coating was only generated to cover the whole surface of the OCGN by the BISA, which hardly affected the inner structure of the OCGN. In addition, by controlling soaking time during boiling, the adhesion force of the PP/OGCN for the droplets can be tuned. The superhydrophobic PP/OGCN as a sensor was able to detect the size of falling droplets according to the variation of resistance (Fig. 14d). When a droplet was dripped on the PP/OGCN, water vapor molecules interacted with the inner graphene through the porous network, thus resulting in the charge transfer between water vapor molecules and graphene, which led to the increase of the resistance (Fig. 14e). The larger the size of the droplet was, the greater the variation of resistance became. The developed BISA strategy may provide an alternative way to generate surfaces with superwettability to achieve multiple functions including self-cleaning and raindrops detecting.

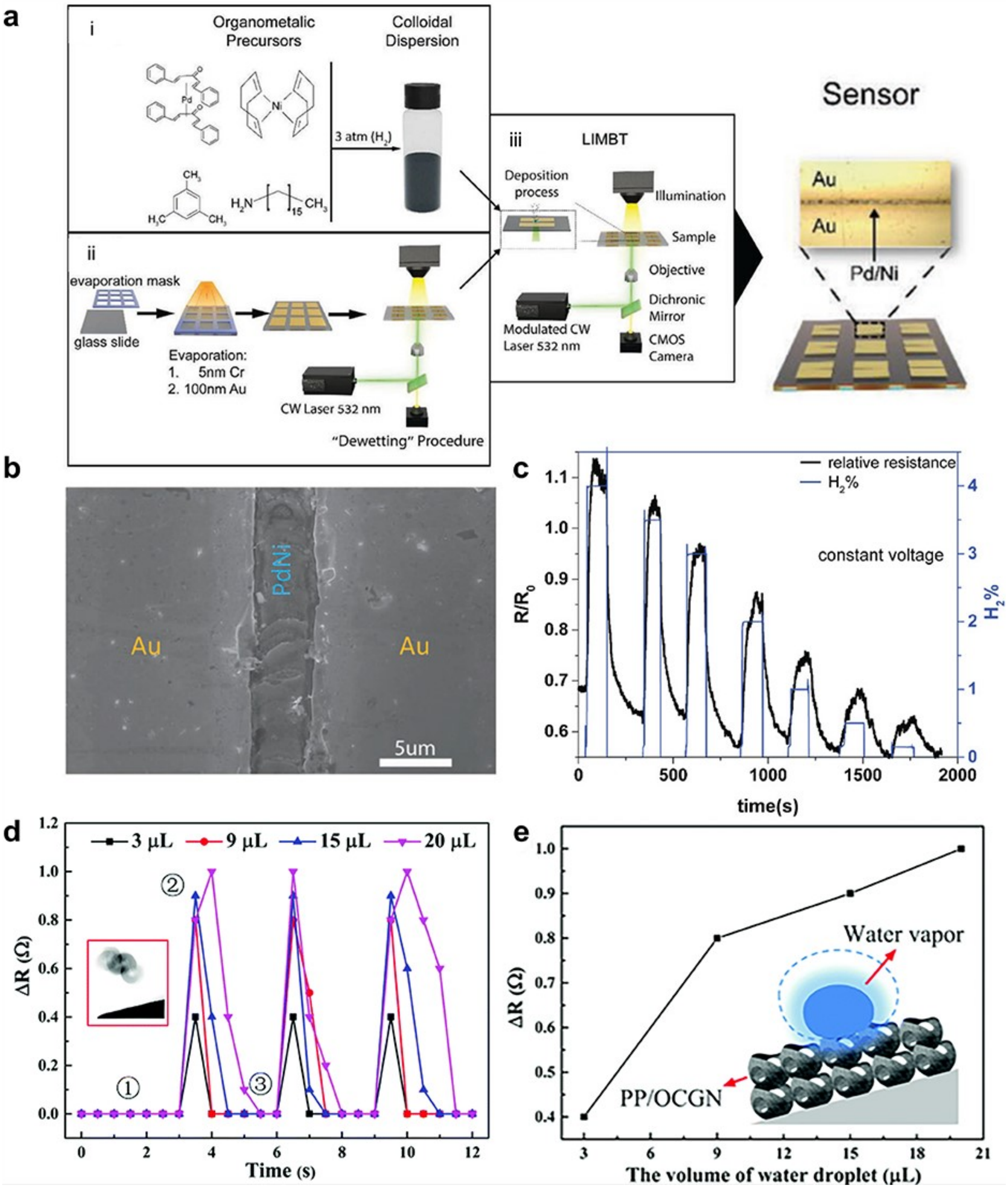

Fig. 14. BISA for gas and liquid sensors. (a) Generation procedures of hydrogen sensors by one-step laser-generated BISA. (b) SEM image of the palladium/nickel structure on the gold substrate by the BISA. (c) Generated sensors response to various concentration of hydrogen at constant voltage in air. Reproduced with permission.[128] Copyright 2019, Wiley-VCH. Superhydrophobic coating surfaces for detecting falling droplets. (d) Resistance variation of the PP/OCGN when different volume of water droplets dropped on the surface. Inset image depicted that a droplet bounced from the surface. (e) Relationship between the volume of water droplet and the change of resistance of the PP/OCGN. Reproduced with permission.[129] Copyright 2018, Royal Society of

Chemistry.

6.3 BISA for catalysis

Metal-based nanoalloys have shown improved catalytic performance over single component.[130] The generation of these nanoalloys, however, is quite difficult due to the complex preparation techniques.[131] Laser-generated microbubbles can provide a nanoscale space with high temperature and pressure to accumulate the chemical precursors and generate metal-based nanoalloys without postprocessing. Rhodium-gold nanoalloy patterns with different line spacing of 4 μm and 2 μm can be fabricated by the laser-generated BISA of mixed rhodium-gold precursor solution, respectively (Fig. 15a and Fig. 15b).[132] To characterize the catalytic performance of the nanoalloys, studies about the reduction of p-nitrophenol have been conducted. According to the UV-vis adsorption spectrum, different catalysts including gold, rhodium and rhodium-gold nanoalloy showed reduction reaction (Fig. 15c). By comparison, rhodium-gold nanoalloy by the BISA had a higher conversion percentage of reactants over individual metal, which demonstrated favorable catalytic performance of the nanoalloy (Fig .15d).

In addition, a patterned chip as catalyst was generated by the BISA of soft oxometalate (SOM)-porous organic framework (POF) dispersion.[133] The generated patterned chip of SOM-POF composite was shown in Fig. 15e. The catalytic performance of the patterned chip has been tested, which showed high catalytic activity compared to the benchmark molecular catalysts due to highly accessible mesopores on the SOM-POF composite. The catalytic ability of patterned chip has been further quantified based on the Raman spectroscopy when the chip was used for catalyzing the oxidation of benzaldehyde to benzoic acid. The peak intensity of catalytic reaction products only increased with time on the trail site, which showed the site-specific characteristic of the catalysis (Fig. 15f).

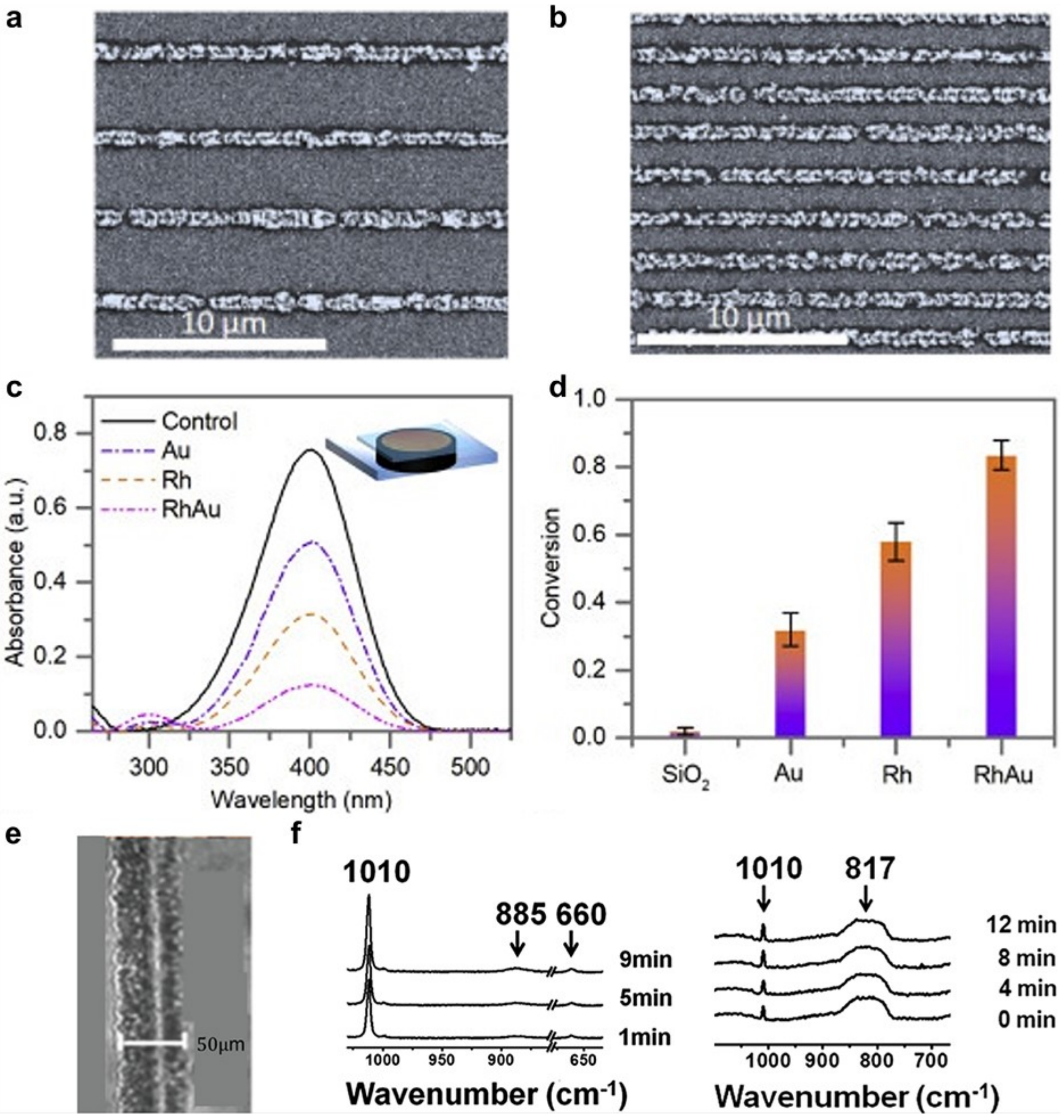

Fig. 15. BISA for catalysis. SEM images of rhodium-gold nanoalloys with different line spacing of (a) 4 µm and (b) 2 µm by the BISA, respectively. (c) UV-vis absorption spectra showing the reduction of p-nitrophenol when generated rhodium-gold nanoalloys by the BISA are used as catalysts. (d) Comparison in conversion percentage of reactants between SiO_2, gold, rhodium, and rhodium-gold nanoalloys as catalysts. Reproduced with permission.[132] Copyright 2019, Elsevier. (e) SEM image of SOM-POF composites generated by the BISA for catalysis from benzaldehyde into benzoic acid. (f) Raman spectroscopy demonstrating catalysis at SOM-POF trail site (left figure) and no catalysis away from SOM-POF trail site (right figure). Reproduced with permission.[133] Copyright 2015, Royal Society of Chemistry.

These works demonstrate that the facile and low-cost BISA strategy can controllably generate films with nanoengineered surfaces and desired properties for a variety of energy-related applications. Fig. 16 shows the extended practical applications in the future development. On the one hand, The BISA strategy discussed in this work plays a key role in the enhancement of phase-change heat transfer, which exhibits potential in traditional energy-related applications such as power generation, thermal managements of high-power-density electronics and seawater desalination.[134-136] On the other hand, the BISA method can facilitate the generation of films with superwettability, which may be promising in the solar cell,[137] anticorrosion,[138] and anti-icing[139, 140]. It should also be mentioned that films with multifunctional properties generated by the BISA have been just tested in the laboratories rather than being proved to be durable and scalable for industrial applications.

Fig. 16. Extended applications of films with nanoengineered surfaces via the BISA in the future. Reproduced with permission.[135] Copyright 2020, Springer Nature. Reproduced with permission.[138] Copyright 2022, American Chemical Society.

7. Conclusions and prospects

In this review, we have summarized recent progress of films with nanoengineered surfaces generated by the BISA strategy toward energy-related applications. We first introduce the underlying mechanism of the BISA, then discuss the regulation methods for generating films with different surface structures and characteristics, and further focus on the application of the BISA strategy for high-performance phase-change heat transfer in recent researches. Also, the relationship between the enhanced boiling heat transfer capacity and the surface characteristics including wettability, roughness and capillary wicking, which can influence bubble dynamics, is discussed in detail. The films can not only be generated on the plain surface by the BISA strategy, but also combine with the existing micro/nanostructured surfaces to further enhance boiling heat transfer capacity. Then, the advanced methods for the BISA by femtosecond laser and the BISA at air-liquid interface to fabricate distinct structures and materials are newly developed. Furthermore, the BISA strategy can be used to generate large-scale films on various target substrates such as polymer, metal, glass and silicon. Various energy-related applications of the BISA, which involve the supercapacitor, smart sensors, electronics cooling, high-power thermal management and solar cell, are demonstrated.

Despite many great efforts, some challenges still remain in the development of the BISA. During the BISA, the stability of nanofluid containing nanomaterials is key for the generation of uniform films on the substrate. To ameliorate this problem, using surfactants and tuning the pH value of nanofluids to improve stability may be alternative approaches. Besides the generation technology, the stability and durability of the films by the BISA are quite important to practical applications, especially under the harsh working environment. The durability of the films generated by the BISA, however, are scarcely studied. In the future development, pursuing stable and durable films by using nanomaterials with excellent performance during the BISA is desired.

Enhancing the performance of phase-change heat transfer is crucial to enable highly efficient thermal management in many energy-related applications. A very clear and comprehensive mechanism for explaining the enhanced performance is still lacking. The accurate theoretical models to predict the phase-change heat transfer process need further exploration, which will facilitate the design and fabrication of films with nanoengineered surfaces by the BISA. Moreover, although it has been mentioned that the films can be generated by the BISA strategy at the solid-liquid interface or air-liquid interface, few researches consider the BISA process at the liquid-liquid interface. From the perspective of the BISA process, it is also possible to apply external impacts including magnetic field and electric field to help nanomaterials self-assemble to form films with different nanoengineered surfaces on the substrate.

Author contributions

Ben Chu: Methodology and Writing original draft. Ruitong Wang and Weizheng Cheng: Methodology. Tao Peng, Chengyi Song and Wen Shang: Writing - review & editing. Benwei Fu and Tao Deng: Funding acquisition, Writing - review & editing and Supervision.

Acknowledgements

We thanks the funding support from the National Natural Science Foundation of China (Grant Nos. 51873105 and 51973109), Project from Ministry of Science and Technology of China (Grant No. 2022YFA1203100), and Innovation Program of Shanghai Municipal Education Commission (Grant No. 2019-01-07-00-02-E00069).

References

1 A. Mazzone, D. K. F. Cruz, S. Tumwebaze, M. Ushigua, P. A. Trotter, A. E. Carvajal , R. Schaeffer and R. Khosla, *Nat. Energy*, 2023, **8**, 19-29.

2 X. Hu, D. Zuo, S. Cheng, S. Chen, Y. Liu, W. Bao, S. Deng, S. J. Harris and J. Wan, *Chem. Soc. Rev.*, 2023, **52**, 1103-1128.

3 S. Yu, Y. Gu, X. Chao, G. Huang and D. Shou, *J. Mater. Chem. A*, 2023, **11**, 5978-6015.

4 K. Liang, L. Li and Y. Yang, *ACS Energy Lett.*, 2017, **2**, 373-390.

5 B. Xu, Q. Wang, Q. Meng, M. He, C. Guo, L. Jiang and H. Liu, *Adv. Funct. Mater.*, 2019, **29**, 1900487.

6 J. Lee, Y. Suh, M. Kuciej, P. Simadiris, M. T. Barakoc and Y. Won, *Nanoscale*, 2022, **14**, 13078-13089.

7 J. Li, G. Zhu, D. Kang, W. Fu, Y. Zhao and N. Miljkovic, *Adv. Funct. Mater.*, 2020, **31**, 2006249.

8 X. Yan, W. Xu, Y. Deng, C. Zhang, H. Zheng, S. Yang, Y. Song, P. Li, X. Xu, Y. Hu, L. Zhang, Z. Yang, S. Wang and Z. Wang, *Sci. Adv.*, 2022, **8**, eabo7698.

9 F. Wu, H. Ze, S. Chen and X. Gao, *ACS Appl. Mater. Interfaces*, 2020, **12**, 39902-39909.

10 X. Yuan, Y. Du and J. Su, *Renew. Sust. Energ. Rev.*, 2022, **156**, 111974.

11 Y. Song, C. Wang, D. J. Preston, G. Su, M. M. Rahman, H. Cha, J. H. Seong, B. Philips, M. Bucci and E. N. Wang, *ACS Appl. Mater. Interfaces*, 2022, **14**, 9788-9794.

12 D. Lorfing, R. Olives, Q. Falcoz, E. Guillot, C. L. Men and A. Ahmadi, *Energy Convers. Manage.*, 2021, **249**, 114835.

13 X. Wang, J. Yang, Q. Wen, S. Shittu, G. Liu, Z. Qiu, X. Zhao and Z. Wang, *Appl. Energy*, 2022, **322**, 119451.

14 H. J. Cho, D. J. Preston, Y. Zhu and E. N. Wang, *Nat. Rev. Mater.*, 2016, **2**, 16092.

15 R. Wen, X. Ma, Y. C. Lee and R. Yang, *Joule*, 2018, **2**, 2307-2347.

16 Y. Sun, Y. Tang, S. Zhang, W. Yuan and H. Tang, *Renew. Sust. Energ. Rev.*, 2022, **162**, 112437.

17 N. V. Upot, K. F. Rabbi, S. Khodakarami, J. Y. Ho, J. K. Mendizabal and N. Miljkovic, *Nanoscale Adv.*, 2023, **5**, 1232-1270.

18 Z. Xu, P. Zhang, C. Yu, W. Miao, Q. Chang, M. Qiu, Y. Li, Y. Tian and L. Jiang, *Adv. Mater.*, 2023, 2210557.

19 S. Zhang, X. Jiang, Y. Li, G. Chen, Y. Sun, Y. Tang and C. Pan, *Energy Convers. Manage.*, 2020, **209**, 112665.

20 G. Chen, X. Jiang, Y. Li, J. Bai, S. Waqar Ali Shah, Y. Gao, Y. Tang, S. Zhang and C. Pan, *Energy Convers. Manage.*, 2023, **277**, 116688.

21 N. Saneie, V. Kulkarni, K. Fezzaa, N. A. Patankar and S. Anand, *ACS Appl. Mater. Interfaces*, 2022, **14**, 15774-15783.

22 K. N. R. Sinha, V. Kumar, N. Kumar, A. Thakur and R. Raj, *Cell Rep. Phys. Sci.*, 2021, **2**, 100382.

23 Q. N. Pham, S. Zhang, S. Hao, K. Montazeri, C. H. Lin, J. Lee, A. Mohraz and Y. Won, *ACS Appl. Mater. Interfaces*, 2020, **12**, 19174-19183.

24 J. Li, Y. Zhao, J. Ma, W. Fu, X. Yan, K. F. Rabbi and N. Miljkovic, *Adv. Funct. Mater.*, 2021, **32**, 2108836.

25 J. Li, W. Fu, B. Zhang, G. Zhu and N. Miljkovic, *ACS Nano*, 2019, **13**, 14080-14093.

26 D. Kong, M. Kang, K. Y. Kim, J. Jang, J. Cho, J. B. In and H. Lee, *ACS Appl. Mater. Interfaces*, 2020, **12**, 37784-37792.

27 M. Moze, M. Senegacnik, P. Gregorcic, M. Hocevar, M. Zupancic and I. Golobic, *ACS Appl. Mater. Interfaces*, 2020, **12**, 24419-24431.

28 C. Salmean and H. Qiu, *Nano Lett.*, 2022, **22**, 8487-8494.

29 B. Yuan, L. Liu, C. Cui, J. Fang, Y. Zhang and J. Wei, *ACS Appl. Mater. Interfaces*, 2021, **13**, 48189-48195.

30 Y. Song, C. D. D. Marin, L. Zhang, H. Cha, Y. Zhao and E. N. Wang, *Adv. Mater.*, 2022, **34**, 2200899.

31 D. I. Shim, G. Choi, N. Lee, T. Kim, B. S. Kim, and H. H. Cho, *ACS Appl. Mater. Interfaces*, 2017, **9**, 17595-17602.

32 D. J. Guckenberger, T. E. de Groot, A. M. Wan, D. J. Beebe and E. W. Young, *Lab Chip*, 2015, **15**, 2364-2378.

33 W. Zhou, X. Hu, L. Mao and Y. He, *Appl. Therm. Eng.*, 2020, **165**, 114396.

34. S. Sudhakar, J. A. Weibel, F. Zhou, E. M. Dede and S. V. Garimella, *Int.. J. Heat Mass Transf.*, 2019, **135**, 1346-1356.

35 C. M. Patil, K. S. V. Santhanam and S. G. Kandlikar, *Int. J. Heat Mass Transf.*, 2014, **79**, 989-1001.

36 H. Seo, H. D. Yun, S. Y. Kwon and I. C. Bang, *Nano Lett.*, 2016, **16**, 932-938.

37 S. Lee, G. H. Seo, S. Lee, U. Jeong, S. J. Lee, S. J. Kim and W. Choi, *Carbon*, 2016, **107**, 607-618.

38 A. Sitar, M. Može, M. Crivellari, J. Schille and I. Golobič, *Int. J. Heat Mass Transf.*, 2020, **147**, 118956.

39 H. Zhao, S. Dash, N. S. Dhillon, S. Kim, B. Lettiere, K. K. Varanasi and A. J. Hart, *ACS Appl. Nano Mater.*, 2019, **2**, 5538-5545.

40 Z. Dai, Y. Li, G. Duan, L. Jia and W. Cai, *ACS Nano*, 2012, **6**, 6706-6716.

41 H. Liu, Y. Zhao, Y. Liu, T. Liang, Y. Tian, T. Sakthivel, S. Peng, S. Y. Kim and Z. Dai, *Chem. Commun.*, 2023, **59**, 2931-2934.

42 H. Chen, Y. Zhang, L. Huang, X. Zhao, X. Ma, Z. Ma, J. Hou, J. Wei, P. D. Marco, O. Mahian and N. Hao, *Chem. Eng. J.*, 2023, **465**, 142799.

43 B. Chu, C. Fang, F. Zheng, W. Cheng, R. Wang, W. Zhang, J. Tao, L. Huai, P. Tao, C. Song, W. Shang, B. Fu and T. Deng, *Mater. Today Energy*, 2021, **22**, 100868.

44 S. A. Khan, M. Koç□ and S. G. Al-Ghamdi, *Energy Convers. Manage.*, 2020, **222**, 113244.

45 C. G. J. Prakash and R. Prasanth, *Renew. Sust. Energ. Rev.*, 2018, **82**, 4028-4043.

46 S. Ridwan, J. Pollack and M. McCarthy, *Langmuir*, 2021, **37**, 6107-6114.

47 J. H. Kim, J. M. Kim, G. W. Lee, G. H. Shim, S. T. Lim, K. M. Kim, T. T. N. Vo, B. Kweon, S. Wongwises, D. W. Jerng, M. H. Kim and H. S. Ahn, *ACS Nano*, 2021, **15**, 2839-2848.

48 Z. Shi, P. He, N. Wang, Y. Liu, X. Chen, Y. Li, G. Ding, Q. Yu and X. Xie, *Adv. Funct. Mater.*, 2022, **32**, 2203124.

49 A. V. Moghadam, H. R. Goshayeshi, I. Chaer, A. Paurine, S. Z. Heris and H. Pourpasha, *Int. J. Energy Res.*, 2022, **46**, 19882-19893.

50 L. Zhang, C. Wang, G. Su, A. Kossolapov, G. Matana Aguiar, J. H. Seong, F. Chavagnat, B. Phillips, M. M. Rahman and M. Bucci, *Nat. Commun.*, 2023, **14**, 2321.

51 C. D. D. Marín, D. Li, F. J. V. Cosme, S. Pajovic, H. Cha, Y. Song, C. Kilpatrick, G. Vaartstra, C. T. Wilson, S. Boriskina and E. N. Wang, *Nano Lett.*, 2023, **23**, 1888-1896.

52 S. Lim and D. Wasan, *J. Colloid Interface Sci.*, 2017, **500**, 96-104.

53 T. Wei and F. Duan, *Phys. Fluids*, 2016, **28**, 124106.

54 J. Wang and G. Liang, *Chem. Eng. Sci.*, 2023, **270**, 118547.

55 A. Inbaoli, C. S. Sujith Kumar and S. Jayaraj, *Appl. Therm. Eng.*, 2022, **214**, 118805.

56 B. Chu, B. Fu, L. Dong, W. Cheng, R. Wang, F. Zheng, C. Fang, P. Tao, C. Song, W. Shang and T. Deng, *Nano Lett.*, 2023, **23**, 259-266.

57 X. Fang, Y. Chen, H. Zhang, W. Chen, A. Dong and R. Wang, *Renew. Sust. Energ. Rev.*, 2016, **62**, 924-940.

58 M. Goodarzi, I. Tlili, H. Moria, E. M. Cardoso, T. A. Alkanhal, A. E. Anqi and M. R. Safaei, *Powder Technol.*, 2021, **377**, 10-19.

59 B. Chu, F. Zheng, C. Fang, R. Wang, W. Cheng, J. Tao, W. Zhang, P. Tao, C. Song, W. Shang, J. Cao, B. Fu and T. Deng, *Int. J. Heat Mass Transf.*, 2022, **197**, 123384.

60 X. Ma, Y. Song, Y. Wang, S. Yao and K. Vafai, *Powder Technol.*, 2022, **397**, 117110.

61 S. M. Kwark, G. Moreno, R. Kumar, H. Moon and S. M. You, *Int. J. Heat Mass Transf.*, 2010, **53**, 4579-4587.

62 I. S. Kiyomura, L. L. Manetti, A. P. da Cunha, G. Ribatski and E. M. Cardoso, *Int. J. Heat Mass Transf.*, 2017, **106**, 666-674.

63 Z. Zhang, J. Wang, J. Shang, Y. Xu, Y. Wan, Z. Lin, R. Sun and Y. Hu, *Small*, 2023, **19**, 2205716.

64 A. Nisar, L. Lou, B. Boesl and A. Agarwal, *Carbon*, 2023, **205**, 573-582.

65 P. Mao, J. Qiao, Y. Zhao, S. Jiang, K. Cui, J. Qiu, K. Tai, J. Tan and C. Liu, *Carbon*, 2021, **172**, 712-719.

66 L. Mao, X. Hu and W. Zhou, *Carbon*, 2020, **164**, 184-197.

67 N. Sezer, S. A. Khan and M. Koç, *Energy Technol.*, 2020, **8**, 2000532.

68 Y. Song, X. Ma, Y. Wang, S. Yao and K. Vafai, *Energy Convers. Manage.: X*, 2021, **12**, 100109.

69 N. Sezer, S. A. Khan and M. Koç, *Int. J. Heat Mass Transf.*, 2019, **145**, 118732.

70 M. Dadhich and O. S. Prajapati, *Renew. Sust. Energ. Rev.*, 2019, **112**, 607-625.

71 X. Li, I. Cole and J. Tu, *Int. J. Heat Mass Transf.*, 2019, **141**, 20-33.

72 Y. Wang, K. Deng, J. Wu, G. Su and S. Qiu, *Int. J. Heat Mass Transf.*, 2020, **158**, 119985.

73 X. Quan, D. Wang and P. Cheng, *Int. J. Heat Mass Transf.*, 2017, **108**, 32-40.

74 Y. Kim, H. Ding and Y. Zheng, *Nano Lett.*, 2020, **20**, 7020-7027.

75 B. B. Rajeeva, L. Lin, E. P. Perillo, X. Peng, W. W. Yu, A. K. Dunn and Y, Zheng, *ACS Appl. Mater. Interfaces*, 2017, **9**, 16725-16733.

76 H. S. Ahn, J. W. Jang, M. Seol, J. M. Kim, D. J. Yun, C. Park, H. Kim, D. H. Youn, J. Y. Kim, G. Park, S. C. Park, J. M. Kim, D. I. Yu, K. Yong, M. H. Kim and J. S. Lee, *Sci. Rep.*, 2013, **3**, 1396.

77 S. M. Kwark, R. Kumar, G. Moreno, J. Yoo and S. M. You, *Int. J. Heat Mass Transf.*, 2010, **53**, 972-981.

78 W. K. Hwang, S. Choy, S. L. Song, J. Lee, D. S. Hwang and K. Y. Lee, *Carbohydr. Polym.*, 2019, **213**, 393-402.

79 L. Zhang, J. H. Seong and M. Bucci, *Phys. Rev. Lett.*, 2019, **122**, 134501.

80 X. Dai, P. Wang, F. Yang, X. Li and C. Li, *Appl.Phys. Lett.*, 2018, **112**, 253901.

81 R. Wen, Q. Li, W. Wang, B. Latour, C. H. Li, C. Li, Y. C. Lee and R. Yang, *Nano Energy*, 2017, **38**, 59-65.

82 Z. Wu, Z. Cao and B. Sundén, *Appl. Energy*, 2019, **249**, 286-299.

83 S. Shin, G. Choi, B. Rallabandi, D. Lee, D. I. Shim, B. S. Kim, K. M. Kim and H. H. Cho, *Nano Lett.*, 2018, **18**, 6392-6396.

84 W. Zhou, L. Mao, X. Hu and Y. He, *Carbon*, 2019, **150**, 168-178.

85 Y. S. Lim and Y. M. Hung, *Energy Convers. Manage.*, 2021, **244**, 114522.

86 H. S. Ahn, J. M. Kim, C. Park, J. W. Jang, J. S. Lee, H. Kim, M. Kaviany and M. H. Kim, *Sci. Rep.*, 2013, **3**, 1960.

87 H. Seo, J. H. Chu, S. Y. Kwon and I. C. Bang, *Int. J. Heat Mass Transf.*, 2015, **82**, 490-502.

88 R. Kumara and D. Milanova, *Appl. Phys. Lett.*, 2009, **94**, 073107.

89 N. Zuber, *Trans. ASME*, 1958, **80**, 711-720.

90 C. Zhang, J. W. Palko, M. T. Barako, M. Asheghi, J. G. Santiago and K. E. Goodson, *Adv. Funct. Mater.*, 2018, **28**, 1803689.

91 K. H. Chu, Y. Soo Joung, R. Enright, C. R. Buie and E. N. Wang, *Appl. Phys. Lett.*, 2013, **102**, 151602.

92 R. Wen, S. Xu, Y. C. Lee and R. Yang, *Nano Energy*, 2018, **51**, 373-382.

93 L. Zhang, T. Wang, S. Kim, S. Tan and Y. Jiang, *Appl. Phys. Lett.*, 2019, **115**, 103701.

94 X. Zhang, H. Liu and L. Jiang, *Adv. Mater.*, 2019, **31**, 1804508.

95 G. Yang, J. Liu, X. Cheng, Y. Wang, X. Chu, S. Mukherjee, A. Terzis, A. Schneemann, W. Li, J. Wu and R. A. Fischer, *J. Mater. Chem. A*, 2021, **9**, 25480-25487.

96 H. J. Cho, J. P. Mizerak and E. N. Wang, *Nat. Commun.*, 2015, **6**, 8599.

97 S. Ridwan and M. McCarthy, *ACS Appl. Mater. Interfaces*, 2019, **11**, 12441-12451.

98 Y. Hu, Y. Lei, X. Liu and R. Yang, *Mater. Today Phys.*, 2022, **28**, 100857.

99 F. Zhang and A. M. Jacobi, *Colloid Surf. A*, 2016, **506**, 438-444.

100 K. Yang, J. Shi, L. Wang, Y. Chen, C. Liang, L. Yang and L. N. Wang, *J. Mater. Sci. Technol.*, 2022, **99**, 82-100.

101 D. Ciloglu and A. Bolukbasi, *Appl. Therm. Eng.*, 2015, **84**, 45-63.

102 W. Li, R. Dai, M. Zeng and Q. Wang, *Renew. Sust. Energ. Rev.*, 2020, **130**, 109926.

103 H. H. Son, G. H. Seo, U. Jeong, D. Y. Shin and S. J. Kim, *Int. J. Heat Mass Transf.*, 2017, **113**, 115-128.

104 H. D. Kim and M. H. Kim, *Appl. Phys. Lett.*, 2007, **91**, 014104.

105 S. M. Kwark, M. Amaya, R. Kumar, G. Moreno and S. M. You, *Int. J. Heat Mass Transf.*, 2010, **53**, 5199-5208.

106 L. Zhang, C. Wang, G. Su, A. Kossolapov, G. M. Aguiar, J. H. Seong, F. Chavagnat, B. Phillips,

M. M. Rahman and M. Bucci, *Nat. Commun.*, 2023, **14**, 2321.

107 L. Mao, W. Zhou, X. Hu, Y. He, G. Zhang, L. Zhang and R. Fu, *Int. J. Therm. Sci.* 2020, **147**, 106154.

108 S. A. Khan, N. Sezer and M. Koç, *Appl. Therm. Eng.*, 2019, **153**, 168-180.

109 H. Chu, N. Xu, X. Yu, H. Jiang, W. Ma and F. Qiao, *Appl. Therm. Eng.*, 2022, **215**, 119041.

110 G. Choi, D. I. Shim, D. Lee, B. S. Kim and H. H. Cho, *Int. Commun. Heat Mass Transf.*, 2019, **109**, 104331.

111 G. Choi, M. Yun, W. T. Hsu, D. I. Shim, D. Lee, B. S. Kim and H. H. Cho, *Int. J. Heat Mass Transf.*, 2022, **197**, 123329.

112 S. Mori, S. Mt Aznam and K. Okuyama, *Int. J. Heat Mass Transf.*, 2015, **80**, 1-6.

113 E. H. Hill, C. Goldmann, C. Hamon and M. Herber, *J. Phys. Chem. C*, 2022, **126**, 7622-7629.

114 S. Ghosh, A. D. Ranjan, S. Das, R. Sen, B. Roy, S. Roy and A. Banerjee, *Nano Lett.*, 2021, **21**, 10-25.

115 L. Lin, X. Peng, Z. Mao, W. Li, M. N. Yogeesh, B. B. Rajeeva, E. P. Perillo, A. K. Dunn, D. Akinwande and Y. Zheng, *Nano Lett.*, 2016, **16**, 701-708.

116 P. S. Kollipara, R. Mahendra, J. Li and Y. Zheng, *Aggregate*, 2022, **3**, e189.

117 Y. Xie and C. Zhao, *Nanoscale*, 2017, **9**, 6622.

118 Q. Zhang, Y. Pang, J. Schiffbauer, A. Jemcov, H. C. Chang, E. Lee and T. Luo, *ACS Appl. Mater. Interfaces*, 2019, **11**, 48525-48532.

119 N. Armon, E. Greenberg, E. Edri, O. N. Avramovitz, Y. Elias and H. Shpaisman, *Adv. Funct. Mater.*, 2021, **31**, 2008547.

120 M. Herber, D. Lengle, S. R. Valandro, M. Wehrmeister and E. H. Hill, *Nano Lett.*, 2023, **23**, 6308-6314.

121 X. Li, Q. Zheng, C. Li, G. Liu, Q. Yang, Y. Wang, P. Sun, H. Tian, C. Wang, X. Chen and J. Shao, *Adv. Energy Mater.*, 2023, 2203761.

122 M. F. E. Kady, Y. Shao and R. B. Kaner, *Nat. Rev. Mater.*, 2016, **1**, 16033.

123 S. A. Khan, N. Sezer, S. Ismail and M. Koç, *Energy Convers. Manage.*, 2019, **195**, 1056-1066.

124 A. Hasan, J. Sarwar and A. H. Shah, *Renew. Sust. Energ. Rev.*, 2018, **94**, 835-852.

125 Z. Li, S. Fang, H. Sun, R. J. Chung, X. Fang and J. H. He, *Adv. Energy Mater.*, 2023, **13**,

2203019.

126 I. Nath, J. Chakraborty, R. Lips, S. Dekyvere, J. Min, R. S. Varma and F. Verpoort, *J. Mater. Chem. A*, 2023, **11**, 10699-10709.

127 Q. Yang, B. Ge, P. Yuan, S. Luo, H. Zhang, Z. Zhao, J. Zhang, S. Wang, X. Bao and X. Yao, *Adv. Funct. Mater.*, 2023, **33**, 2214588.

128 G. Rahamim, E. Greenberg, K. Rajouâ, F. Favier, H. Shpaisman and D. Zitoun, *Adv. Mater. Interfaces*, 2019, **6**, 1900768.

129 G. Ding, W. Jiao, L. Chen, M. Yan, L. Hao and R. Wang, *J. Mater. Chem. A*, 2018, **6**, 16992-17000.

130 P. Lu, J. Zhou, Y. Hu, J. Yin, Y. Wang, J. Yu, Y. Ma, Z. Zhu, Z. Zeng and Z. Fan, *J. Mater. Chem. A*, 2021, **9**, 19025-19053.

131 X. Wang, N. Fu, J. C. Liu, K. Yu, Z. Li, Z. Xu, X. Liang, P. Zhu, C. Ye, A. Zhou, A. Li, L. Zheng, L. M. Liu, C. Chen, D. Wang, Q. Peng and Y. Li, *J. Am. Chem. Soc.*, 2022, **144**, 23223-23229.

132 B. B. Rajeeva, P. Kunal, P. S. Kollipara, P. V. Acharya, M. Joe, M. S. Ide, K. Jarvis, Y. Liu, V. Bahadur, S. M. Humphrey and Y. Zheng, *Matter*, 2019, **1**, 1606-1617.

133 P. Thomas, C. Pei, B. Roy, S. Ghosh, S. Das, A. Banerjee, T. Ben, S. Qiub and S. Roy, *J. Mater. Chem. A*, 2015, **3**, 1431–1441.

134 M. Habibi and L. Cui, *Appl. Energy*, 2023, **343**, 121221.

135 R. V. Erp, R. Soleimanzadeh, L. Nela, G. Kampitsis and E. Matioli, *Nature*, 2020, **585**, 211-216.

136 M. Wang, P. Zhang, X. Liang, J. Zhao, Y. Liu, Y. Cao, H. Wang, Y. Chen, Z. Zhang, F. Pan, Z. Zhang and Z. Jiang, *Nat. Sustain.*, 2022, **5**, 518-526.

137 R. Ji, Z. Zhang, Y. J. Hofstetter, R. Buschbeck, C. Hänisch, F. Paulus and Y. Vaynzof, *Nat. Energy*, 2022, **7**, 1170-1179.

138 C. Zhang, B. Zhang, W. Yuan, O. Yang, Y. Liu, L. He, Z. Zhao, L. Zhou, J. Wang and Z. L. Wang, *ACS Appl. Mater. Interfaces*, 2022, **14**, 8605-8612.

139 S. Li, Y. Hou, M. Kappl, W. Steffen, J. Liu and H. J. Butt, *Adv. Mater.*, 2022, **34**, 2203242.

140 S. Jiang, Y. Diao and H. Yang, *Adv. Colloid Interface Sci.*, 2022, **308**, 102756.